The morphology of the X-ray afterglows and of the jetted GeV emission in long GRBs

R. Ruffini,[1,2,3,4,5]★ R. Moradi,[1,2,6]★ J. A. Rueda [ID],[1,2,7,8,9]★ L. Li,[1,2,6] N. Sahakyan,[10,1] Y.-C. Chen [ID],[1,2] Y. Wang,[1,2,6] Y. Aimuratov,[1,2,11,18] L. Becerra,[1,2,12] C. L. Bianco,[1,2,9] C. Cherubini,[1,13,14] S. Filippi,[1,13,15] M. Karlica,[1,2] G. J. Mathews,[1,16] M. Muccino,[17] G. B. Pisani[1,2] and S. S. Xue[1,2]

[1]*ICRANet, Piazza della Repubblica 10, I-65122 Pescara, Italy*
[2]*ICRA, Dipartimento di Fisica, Università di Roma 'La Sapienza', Piazzale Aldo Moro 5, I-00185 Roma, Italy*
[3]*ICRANet-Rio, Centro Brasileiro de Pesquisas Físicas, Rua Dr. Xavier Sigaud 150, 22290-180 Rio de Janeiro, Brazil*
[4]*Université de Nice Sophia-Antipolis, Grand Château Parc Valrose, 06103 Nice, CEDEX 2, France*
[5]*INAF, Viale del Parco Mellini 84, I-00136 Rome, Italy*
[6]*INAF – Osservatorio Astronomico d'Abruzzo, Via M. Maggini snc, I-64100 Teramo, Italy*
[7]*ICRANet-Ferrara, Dipartimento di Fisica e Scienze della Terra, Università degli Studi di Ferrara, Via Saragat 1, I-44122 Ferrara, Italy*
[8]*Dipartimento di Fisica e Scienze della Terra, Università degli Studi di Ferrara, Via Saragat 1, I-44122 Ferrara, Italy*
[9]*INAF, Istituto di Astrofisica e Planetologia Spaziali, Via Fosso del Cavaliere 100, I-00133 Rome, Italy*
[10]*ICRANet-Armenia, Marshall Baghramian Avenue 24a, Yerevan 0019, Republic of Armenia*
[11]*Fesenkov Astrophysical Institute, Observatory 23, 050020 Almaty, Kazakhstan*
[12]*Instituto de Astrofísica, Facultad de Física, Pontificia Universidad Católica de Chile, Av. Vicuña Mackenna 4860, Macul, 8970117 Santiago, Chile*
[13]*ICRA, University Campus Bio-Medico of Rome, Via Alvaro del Portillo 21, I-00128 Rome, Italy*
[14]*Department of Science and Technology for Humans and the Environment and Nonlinear Physics and Mathematical Modeling Lab, University Campus Bio-Medico of Rome, Via Alvaro del Portillo 21, I-00128 Rome, Italy*
[15]*Department of Engineering, University Campus Bio-Medico of Rome, Nonlinear Physics and Mathematical Modeling Lab, Via Alvaro del Portillo 21, I-00128 Rome, Italy*
[16]*Center for Astrophysics, Department of Physics, University of Notre Dame, Notre Dame, IN 46556, USA*
[17]*Istituto Nazionale di Fisica Nucleare, Laboratori Nazionali di Frascati, I-00044 Frascati, Italy*
[18]*Al-Farabi Kazakh National University, al-Farabi avenue 71, 050040 Almaty, Kazakhstan*

ABSTRACT

We recall evidence that long gamma-ray bursts (GRBs) have binary progenitors and give new examples. Binary-driven hypernovae (BdHNe) consist of a carbon–oxygen core (CO_{core}) and a neutron star (NS) companion. For binary periods ~ 5 min, the CO_{core} collapse originates the subclass BdHN I characterized by (1) an outstanding supernova (SN; the '*SN-rise*'); (2) a black hole (BH), born from the NS collapse by SN matter accretion, leading to a GeV emission with luminosity $L_{GeV} = A_{GeV}\, t^{-\alpha_{GeV}}$, observed only in some cases; and (3) a new NS (νNS), born from the SN, originating from the X-ray afterglow with $L_X = A_X\, t^{-\alpha_X}$, observed in all BdHN I. We record 378 sources and present for four prototype GRBs 130427A, 160509A, 180720B, and 190114C: (1) spectra, luminosities, SN-rise duration; (2) A_X, $\alpha_X = 1.48 \pm 0.32$, and (3) the νNS spin time evolution. We infer (i) A_{GeV}, $\alpha_{GeV} = 1.19 \pm 0.04$ and (ii) the BdHN I morphology from time-resolved spectral analysis, three-dimensional simulations, and the GeV emission presence/absence in 54 sources within the *Fermi*-Large Area Telescope boresight angle. For 25 sources, we give the integrated and time-varying GeV emission, 29 sources have no GeV emission detected and show X/gamma-ray flares previously inferred as observed along the binary plane. The 25/54 ratio implies the GeV radiation is emitted within a cone of half-opening angle $\approx 60°$ from the normal to the orbital plane. We deduce BH masses of 2.3–8.9 $M_\odot$ and spin of 0.27–0.87 by explaining the GeV emission from the BH rotational energy extraction, while their time evolution validates the BH mass–energy formula.

Key words: black hole physics – binaries: general – gamma-ray bursts – transients: supernovae.

1 INTRODUCTION

The year 2021 marks the 50th anniversary of the paper 'Introducing the black hole' (Ruffini & Wheeler 1971) and of the black hole (BH)

mass–energy formula (Christodoulou 1970; Christodoulou & Ruffini 1971; Hawking 1971; Hawking 1972). Since those days, interest in BHs has spread worldwide and their study represents one of the most innovative fields of fundamental physics and astrophysics. There has also been an exponential growth of observational and theoretical developments that are finally reaching the momentous result of unveiling the process of rotational energy extraction from a rotating Kerr BH. We indicate the path of this discovery in

★ E-mail: ruffini@icra.it (RR); rahim.moradi@icranet.org (RM); jorge.rueda@icra.it (JAR)

this paper. This realization has allowed for the identification of the code of gamma-ray bursts (GRBs): one of the most complex sequences of a very large number of non-repetitive classical and quantum events, each of which are characterized by specific spectral and temporal properties. In parallel, a new arena for fundamental physics has been revealed by the dubbed '*blackholic quantum*' (Rueda & Ruffini 2020). This enormous conceptual progress has not been reached straightforwardly: it has come from an intense dedicated process with continuous feedback between theoretical understanding, unprecedented panchromatic observational progress, and modification of basic interpretation paradigms: they have all been truly essential. We first summarize in this introduction some of the contributions which have initiated this most complex inquiry into the the most powerful energy source in the Universe and identify the rotational energy of a Kerr BH as their energy source.

1.1 The initial 'golden age' of relativistic astrophysics

The first breakthrough in relativistic astrophysics was the discovery of pulsars in 1967 (Hewish et al. 1968), and the discovery of a pulsar in the core of the Crab Nebula (Staelin & Reifenstein 1968; Reifenstein, Brundage & Staelin 1969). The identification of the energy source of the pulsar with a fast rotating newly born neutron star (NS); the new NS (νNS), coincident with the supernova (SN) explosion led to a new paradigm in SN understanding (Shklovskij 1969). As we show in this paper, we are gaining a deeper understanding of both of SNe and of the role of the νNS in the binary-driven hypernova (BdHN) systems.

The second breakthrough came from the launch in 1970 of the first X-ray telescope, observing in the 2–20 keV energy band: the *Uhuru* satellite (see e.g. Giacconi & Ruffini 1978; Giacconi 2003). *Uhuru* paved the way for a crucial working method in developing a multiwavelength collaboration with optical and radio observatories. Thanks to the theoretical understanding, this led to the discovery, inside our own galaxy, of a large number of binary X-ray sources composed of a main-sequence star and a companion NS (like Hercules X-1 and Centaurus X-3) and a binary system composed of a main-sequence star and a BH, which gave the first evidence for the discovery of a BH in our Galaxy (see Ruffini 1974; Giacconi & Ruffini 1978, for details). It was soon realized that these binary X-ray sources would themselves further evolve as the companion main-sequence star would undergo an SN explosion on time-scales of 10^8 yr (Ruffini 1974). In view of the limited number of such binary X-ray sources in our Galaxy, the expected observational rate of the final evolution of such binary systems would be of the order of 10^{-8} events per yr in our Galaxy. The point that was missed at the time was the existence of the process of '*induced gravitational collapse*', which was identified years later (Ruffini et al. 2001; Rueda & Ruffini 2012). This implies an unprecedented energy emission of $\sim 10^{54}$ erg, making them observable from all galaxies in the entire Universe: if the number of galaxies in our past light-cone is taken into account, the expected observational rate of the final evolution of such binary X-ray sources in the entire Universe is of the order of 10–100 events per yr. *The third breakthrough* was the introduction in 1971 of the BH mass–energy formula by Christodoulou, Hawking, Ruffini (Christodoulou 1970; Christodoulou & Ruffini 1971; Hawking 1971, 1972), and the BH extractable energy by reversible and irreversible transformation (in geometric $c = G = 1$ units):

$$M^2 = \frac{J^2}{4M_{\rm irr}^2} + M_{\rm irr}^2, \tag{1a}$$

$$S = 16\pi M_{\rm irr}^2 \tag{1b}$$

$$\delta S = 32\pi M_{\rm irr} \delta M_{\rm irr} \geq 0, \tag{1c}$$

where J, M, $M_{\rm irr}$, and S are the angular momentum, mass, irreducible mass, and horizon surface area of the BH, respectively.

Again in this article, we indicate the path to observe for the first time the BH extractable energy process, which can be as high as 29% of the BH mass for an extreme Kerr BH. We measure as well the BH mass and spin in selected BdHN.

Just at the end of this 'initial golden age of relativistic astrophysics', the discovery of GRBs was publicly announced in 1974 February at the annual meeting of the American Association for the Advancement of Science, in San Francisco (see details in Gursky & Ruffini 1975). In that meeting, observations by the Vela 5 and Vela 6 satellites were presented. These satellites operated in the 3–12 keV X-ray energy band and, for the first time, in the 150–750 keV (Vela 5) and 300–1500 keV (Vela 6) gamma-ray energy bands. Tens of gamma-ray events per year of unknown origin, lasting for a few seconds, and originating outside the Solar system, were named 'gamma-ray bursts' (details in Klebesadel, Strong & Olson 1973; Strong 1975).

What has became clear only recently, and further clarified in this article, is that precisely the late catastrophic evolution of the binary X-ray sources leads to the BdHNe: the progenitors of a class of long GRBs. Indeed, these highest luminosity energy sources in the Universe are observed to occur at a rate of 10–100 events per yr, consistent with the order of magnitude estimate given above.

We proceed to focus on the most recent developments, selecting crucial observational milestones, theoretical developments, and define the interpretation paradigms that have recently led to a unified understanding of the GRBs.

1.2 The largest ever multiwavelength observational efforts

The earliest evidence for high-energy radiation above 100 MeV from GRBs was the observations by the Energetic Gamma-Ray Experiment Telescope (*EGRET*), operating in the energy range $\sim$ 20 MeV–30 GeV, onboard of the Compton Gamma-Ray Observatory (*CGRO*, 1991–2000). The detection was triggered by the Burst And Transient Source Experiment (*BATSE*), operating in energy range of $\sim$20–2000 keV. *EGRET* has detected five GRBs that, from our understanding today, were long-duration bursts: GRB 910503, GRB 910601, GRB 930131, GRB 940217, and GRB 940301 (see e.g. Kanbach 1996, and references therein). Unfortunately, no redshift was known at the time.

A new epoch started with the launch of the *Beppo-Sax* satellite in 1996, joining the expertise of the X-ray and gamma-ray communities. Its gamma-ray burst monitor (GRBM) operating in the 40–700 keV energy band determined the trigger of the GRB, and two wide-field cameras operating in the 2–30 keV X-ray energy band allowed the localization of the source to within arcminutes resolution. This enabled a follow-up with the narrow-field instruments (NFI) in the 2–10 keV energy band.

Beppo-SAX achieved three major results:

(i) The discovery of the X-ray afterglow (GRB 970228; Costa et al. 1997), characterized by an X-ray luminosity decreasing with a power law with index of $\alpha_X = -1.48 \pm 0.32$ (see de Pasquale et al. 2006, as well as Li et al. 2015, 2018b; Pisani et al. 2016). In this article, we specifically address the astrophysical origin of the afterglow.

(ii) The determination of the accurate positions by the NFI, transmitted to the optical (van Paradijs et al. 1997) and radio telescopes (Frail et al. 1997), allowed the determination of the GRB cosmological redshifts. The first redshift was measured for GRB 970508 (Metzger et al. 1997), using the LRIS instrument of the Keck II telescope (Oke et al. 1995). The derived distances of ≈5–10 Gpc confirmed their cosmological origin and their unprecedented energetics, ≈10^{50}–10^{54} erg, thus validating our hypothesis derived from first principles (Damour & Ruffini 1975; Ruffini 1998).

(iii) The discovery of the temporal and spatial coincidence of GRB 980425 with SN 1998bw (Galama et al. 1998), which suggested the connection between GRBs and SNe, was soon supported by many additional events (see e.g. Woosley & Bloom 2006; Della Valle 2011; Hjorth & Bloom 2012; Li et al. 2012, 2018a). The astrophysical origin of this coincidence is addressed in this article within the BdHN approach.

The Neil Gehrels *Swift* Observatory (hereafter indicated as *Swift*) followed in 2004. It was conceived as a panchromatic space observatory dedicated to the observations of GRBs. The GRB trigger is detected by the large field of view of its Burst Alert Telescope (BAT; Barthelmy et al. 2005), operating in the hard X-ray band. This is followed up by the fast and automatic observations of the onboard narrow fields instruments XRT (Burrows et al. 2005) and UVOT (Roming et al. 2005) operating in the soft/medium X-ray and in the optical/UV bands, respectively. The BAT telescope operates in the 15–150 keV energy band and can detect the GRB prompt emission while accurately determining its position in the sky within 3 arcmin. Within 90 s, *Swift* can repoint the XRT telescope, operating in the 0.3–10 keV energy range, and relay promptly the burst position to the ground. Unfortunately, this does not allow the establishment of the initial *Swift*-XRT detection prior to the *Swift*-BAT trigger, as later explained in this article.

Thanks to the *Swift* satellite, the number of detected GRBs increased rapidly to 1300 sources with known redshifts (see e.g. Giommi et al. 2020). By analysing the light curve of some long GRBs, Nousek et al. (2006) and Zhang et al. (2006) discovered three power-law segments in the XRT flux light curves prior to the afterglow emission (see also Li et al. 2015, 2018a). We refer in this article to these segments as the 'Nousek–Zhang power laws'. All the X-ray afterglow observations considered in this article refer to *Swift*-XRT observation.

The high-energy astrophysics era of GRB observations started with the launch of *AGILE* in 2007 (Tavani et al. 2009) with the onboard Gamma-Ray Imaging Detector (*GRID*) operating in the 30 MeV–50 GeV energy range. *AGILE* was soon followed by the launch in 2008 June of the *Fermi* satellite, having onboard the gamma-ray burst monitor (GBM) operating in the 8 keV–40 MeV energy range (Meegan et al. 2009) and the Large Area Telescope (LAT) operating in the 20 MeV–300 GeV energy range (Atwood et al. 2009).

AGILE-GRID detected the first long GRB with emission above 100 MeV and with a photometric redshift of $z = 1.8$, GRB 080514B (Giuliani et al. 2008). It was followed four months later by the detection of GRB 080916C (Greiner et al. 2009) by *Fermi* with one of the largest isotropic energies ever detected, $E_{iso} = (4.07 \pm 0.86) \times 10^{54}$ erg, and a photometric redshift of $z = 4.35$. These were followed by a large number of long GRBs observed by LAT with both GeV emission and with a well-defined z. All the high-energy long GRBs considered in this article are based on the first and second *Fermi*-LAT GRB catalogues (Ackermann et al. 2013; Ajello et al. 2019).

The leading observations from space observatories were followed by a multitude of equally essential observations from ground-based observatories spanning the globe. The leading role was taken by the largest optical telescopes, e.g. the VLT from ESO with its X-shooter instrument (Vernet et al. 2011) and radio telescopes. This vastest ever multiwavelength observational campaign has been recently further extended to the very-high-energy (VHE) domain with the GRB detection by observatories on the ground. This is the case of the observations of GRB 190114C by the Imaging Atmospheric Cherenkov Telescopes MAGIC (see Fig. 1 and MAGIC Collaboration 2019a), designed to detect VHE gamma-rays from 30 GeV to more than 50 TeV (see e.g. Aleksić et al. 2016a, b), the observations of GRB 180720B by H.E.S.S (see Fig. 2 and Abdalla et al. 2019), operating in the energy range from tens of GeV to tens of TeV (see e.g. Aharonian et al. 2006), as well as GRB 190829A (Chand et al. 2020), which we also address in this article.

## 1.3 The short GRBs with binary NS progenitors

One of the main results of the observations of the *CGRO* satellite (Murdin 2000) was the isotropic distribution of the GRBs when expressed in galactic coordinates (Meegan et al. 1992). This result gave the first preliminary indication of the cosmological nature of GRBs. This was later confirmed by irrefutable evidence from the observations of *Beppo-Sax*, as mentioned above. An additional result was the clear indication of the existence of two different classes of GRBs: the short and the long GRBs (Kouveliotou et al. 1993). This classification has been confirmed and further extended as we recall in Section 2, now duly expressing all quantities, after *Beppo-Sax*, in the rest frame of the source.

The first proposal of successfully relating a GRB to an astrophysical cosmological source came from the vision of Bohdan Paczynski and collaborators, who identified the progenitors of short GRBs (S-GRBs) with merging NS binaries (see e.g. Paczynski 1986; Eichler et al. 1989; Narayan, Piran & Shemi 1991; Mao & Paczynski 1992; Narayan et al. 1992; Narayan, Paczynski & Piran 1992). This result was later confirmed by *Beppo-Sax* (Li & Paczyński 1998, 2000, 2006; Berger 2014). Complementary information came from the localization of S-GRBs at large off-sets from their host galaxies and with no star formation evidence (see e.g. Fox et al. 2005; Gehrels et al. 2005; Berger 2014). The following fundamental discovery came from the identification of the first S-GRB in the GeV band by *AGILE*. The first observation of an S-GRB was done by *AGILE* who detected GRB 090510A at a spectroscopic redshift of $z = 0.903$, with $E_{iso} = (3.95 \pm 0.21) \times 10^{52}$ erg, and a significant GeV emission $E_{LAT} = (5.78 \pm 0.60) \times 10^{52}$ erg. On the basis of the observed energetics of this source, and its spectral properties, we proposed that in this S-GRB we witness the birth of a BH, which we associate with the onset of the GeV emission: the signature of this event (Ruffini et al. 2016a).

This identification further evolved with the introduction of the two subclasses of short bursts (Ruffini et al. 2015b, 2016a, b; Aimuratov et al. 2017). The first subclass corresponds to short bursts with isotropic energies $E_{iso} < 10^{52}$ erg (in the rest-frame 1–10^4 keV energy band) and rest-frame spectral peak energies $E_{p,i} < 2$ MeV. These are expected to originate when the NS–NS merger leads to a single massive NS (M-NS) with a mass below the NS critical mass. We have called these sources short gamma-ray flashes (S-GRFs).

GRB 190114C
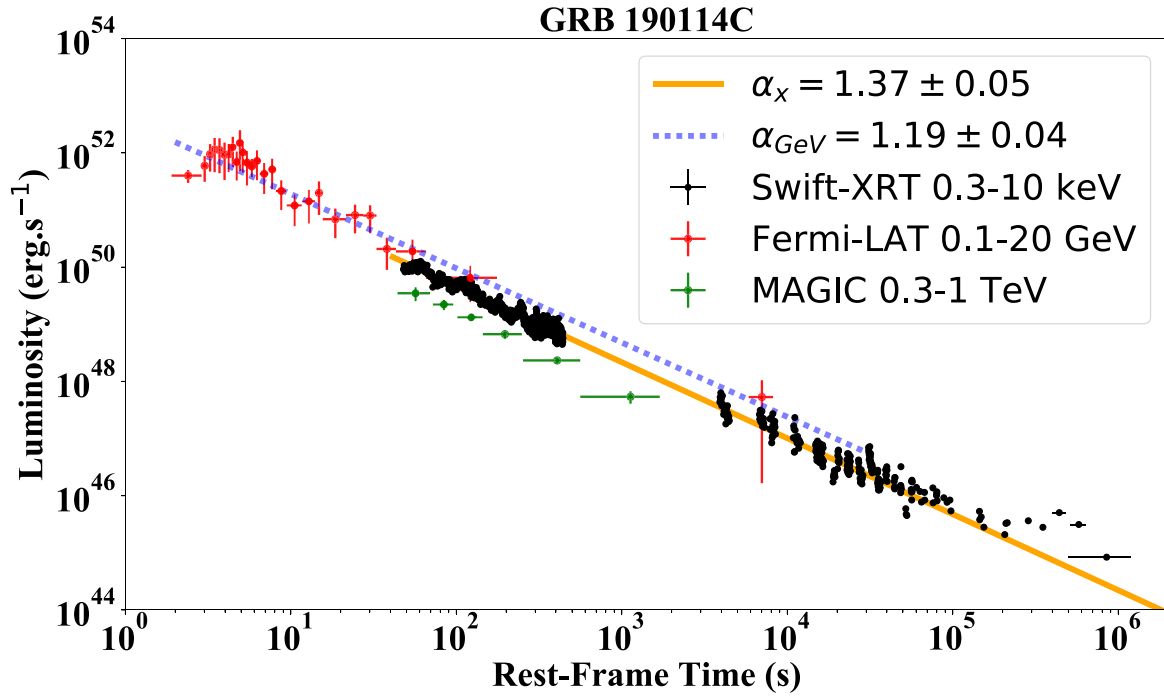
Figure 1. Luminosity of BdHN I 190114C: the black data points represent the rest-frame 0.3–10 keV luminosity obtained from *Swift*-XRT. It follows a decaying power law with index $\alpha_X = 1.37 \pm 0.05$. The red data points show the rest-frame 0.1–20 GeV luminosity observed by *Fermi*-LAT. It follows a decaying power law with amplitude $(4.6 \pm 0.6) \times 10^{52}$ erg s^{-1} and index $\alpha_{GeV} = 1.19 \pm 0.04$. The green data points show the rest-frame 0.3–1 TeV luminosity obtained from MAGIC. Details are given in Sections 4, 5, and 8.

GRB 180720B
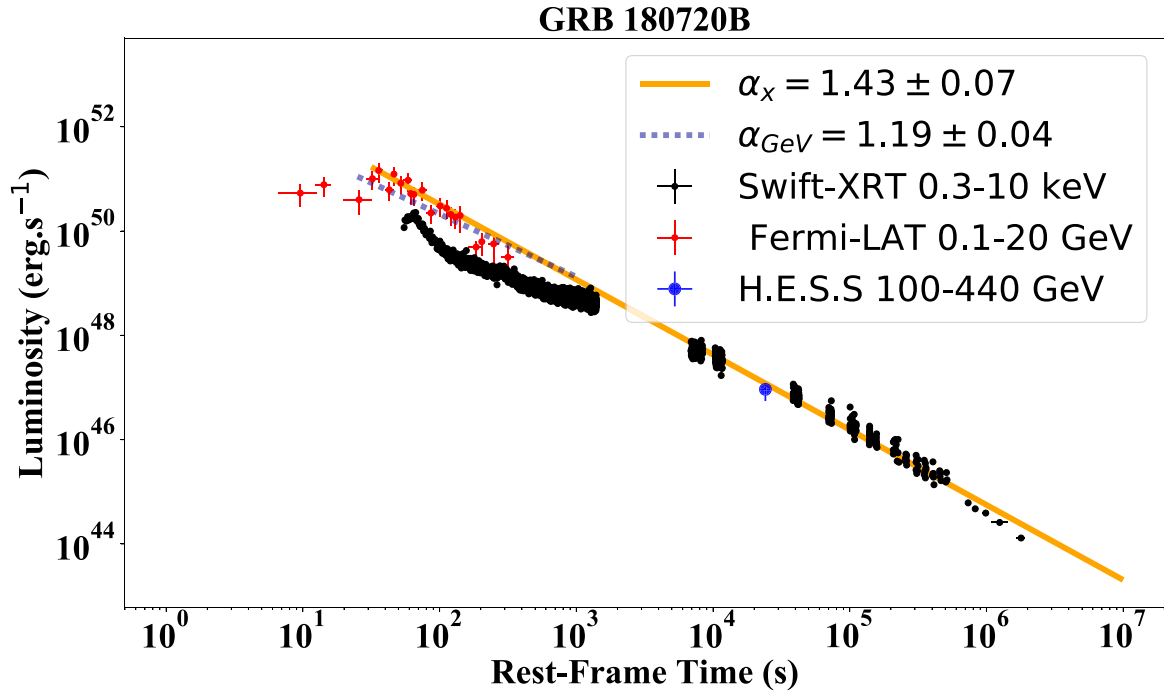
Figure 2. Luminosity of BdHN I 180720B: the black data points represent the rest-frame 0.3–10 keV luminosity obtained from *Swift*-XRT. It follows a decaying power law with index $\alpha_X = 1.43 \pm 0.07$. The blue data point shows the rest-frame 100–440 GeV luminosity observed by H.E.S.S. The red data points show the rest-frame 0.1–20 GeV luminosity observed by *Fermi*-LAT. It follows a decaying power law with amplitude $(5.4 \pm 0.6) \times 10^{52}$ erg s^{-1} and index $\alpha_{GeV} = 1.19 \pm 0.04$. Details are given in Sections 4, 5, and 8.
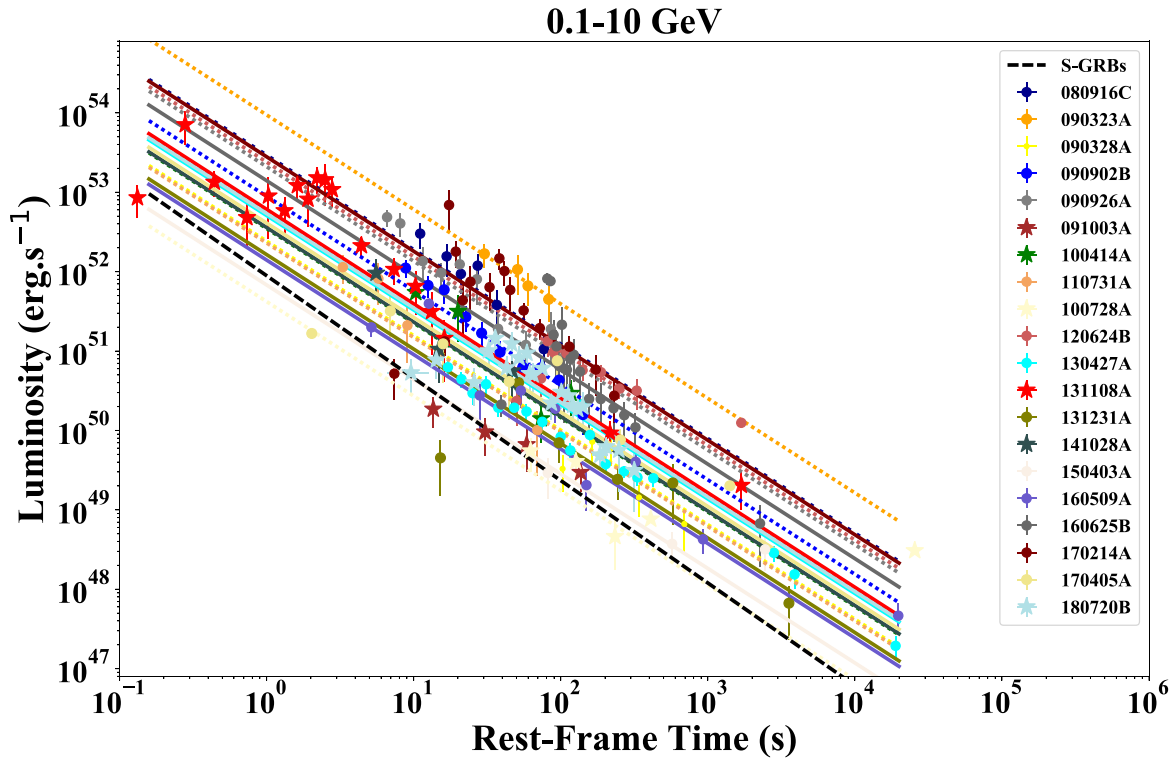
0.1–10 GeV

Figure 3. The rest-frame 0.1–10 GeV isotropic luminosity of 20 selected BdHNe with LAT emission. The solid red line marks the common power-law behaviour of the GeV emission for BdHNe with slope $\alpha_{\rm GeV} = 1.19 \pm 0.04$; the shaded grey area encloses all the luminosity light curves of the selected BdHNe. The dashed black line marks the common power-law behaviour of the GeV emission in S-GRBs with a slope of $\gamma = 1.29 \pm 0.06$.

The second subclass corresponds to short bursts with $E_{\rm iso} \gtrsim 10^{52}$ erg and $E_{\rm p,i} \gtrsim 2$ MeV. It was assumed that these sources, in analogy with the prototype GRB 090510, originate from an NS–NS merger in which the merged core overcomes the NS critical mass and gravitationally collapses to form a BH. We have called these sources genuine S-GRBs (see Ruffini et al. 2016a, 2019c); six of such S-GRBs have been identified, all emitting GeV emission with a decaying luminosity of index $\alpha_{\rm GeV,short} = -1.29 \pm 0.06$ (Ruffini et al. 2019c); see Fig. 3 in Section 8.

We show how, by following these pathfinding works on S-GRBs, we have progressed in formulating the theory of the BdHNe: the theory of long GRBS based on binary progenitors. Before this, however, we summarize the traditional long GRB models based upon a single progenitor.

1.4 Long GRBs in the traditional model

A review of the traditional long GRB model is facilitated by the extensive book by Bing Zhang and many references therein (Zhang 2018). As recounted there, the papers by Rees & Meszaros (1992), Mészáros & Rees (1997), and Woosley (1993) have characterized this traditional model. Rees & Meszaros (1992) proposed a single BH as the origin of GRBs emitting an ultrarelativistic blast wave, whose expansion follows the Blandford–McKee self-similar solution (Blandford & McKee 1976). Woosley (1993) linked the GRB origin to a Kerr BH emitting an ultrarelativistic jet originating from the accretion of toroidal material on to the BH. The BH was assumed to be produced from the direct collapse of a massive star, a 'failed' SN leading to a large BH of approximately 5 M$_\odot$, possibly as high as 10

M$_\odot$, a '*collapsar*'. We will address this interesting idea within our BdHN model in Section 9.

In these ultrarelativistic blast wave models, the afterglow is explained by the synchrotron/synchrotron self-Compton (SSC) emission from accelerated electrons when the blast wave of $\Gamma \sim 1000$ is slowed down by the circumburst medium (Waxman & Piran 1994; Sari & Piran 1995; Sari 1997; Wijers, Rees & Meszaros 1997; Sari, Piran & Narayan 1998).

As pointed out by Zhang (2018), these ultrarelativistic blast wave models have been applied to explain a vast number of observations:

(i) The X-ray afterglow as well as the steep and shallow decay in the 'Nousek–Zhang' phase, the X-ray, and the gamma-ray flares.
(ii) The optical and radio emissions.
(iii) The high-energy emission in the GeV band observed in some long GRBs by *Fermi*-LAT.

An example of this method is the recent case of GRB 190114C, in which the traditional approach has been applied:

(i) To jointly explain the emissions in the TeV observed recently by MAGIC (MAGIC Collaboration 2019a, b; Mirzoyan et al. 2019); see Fig. 1.
(ii) To explain the emission in the MeV and GeV bands observed by the *Fermi* GBM and LAT satellites in the jetted emission.
(iii) To explain the emission in the MeV and keV bands observed by *Swift* including the emission in the optical and radio emissions.

In the traditional model, all of these emissions occur jointly using the kinetic energy of an ultrarelativistic blast wave with Lorentz

Table 1. Alphabetic ordered list of the acronyms used in this work.

Extended wording	Acronym
Binary-driven hypernova	BdHN
Black hole	BH
Carbon–oxygen star	CO-star
Fallback-powered kilonova	FB-KN
Gamma-ray burst	GRB
Gamma-ray flash	GRF
Gamma-ray flash kilonovae	GR-K
Massive neutron star	M-NS
Neutron star	NS
New neutron star	νNS
Short gamma-ray burst	S-GRB
Short gamma-ray flash	S-GRF
Supernova	SN
Supernova rise	SN-rise
Ultrashort gamma-ray burst	U-GRB
White dwarf	WD
X-ray flash	XRF

factor Gamma $\sim 10^3$, emitting at distances of $\sim 10^{16}$–10^{18} cm, implying total energies reaching 10^{55} erg.

This approach, however, encounters some contradictions with model-independent constraints. Moreover, there is no requirement that these different emission processes be explained by a single origin, i.e. the kinetic energy of a blast wave. As we are going to show in this article, each one of the above mentioned emissions finds its reason for existence in different specific processes originating in different specific episodes during the BdHN evolution. Each episode implies a different process and less demanding energy requirements.

1.5 The role of binary systems as progenitors of long GRBs

The role of binary systems as progenitors of long GRBs in our approach involves three assumptions:

(i) That all long GRBs, not only the S-GRBs, originate from binary systems. These binaries are composed of different combinations of CO_{core}, NS, white dwarfs (WDs), BH, and νNS; see Table 1. We classify all GRBs in nine different subclasses on the basis of their energetics, their spectra, and their duration expressed in the rest frame of the source. Only in *some* of these subclasses the presence of a BH occurs (see e.g. Ruffini et al. 2016b, 2018c; Wang et al. 2019); see in detail in Section 2.

(ii) We focus on BdHNe with a binary progenitor composed of a CO-star and a companion binary NS. As the CO_{core} gravitationally collapses, it gives origin to an SN and its iron core collapses to form a νNS. The hypercritical accretion of the SN ejecta on the companion NS leads, for binary periods $\lesssim 5$ min, to the formation of a BH. This happens when the NS critical mass is reached and overcome (Becerra et al. 2016). We denote these systems as BdHNe I in which a BH is formed. The BdHNe I are characterized by an isotropic energy, estimated by the *Fermi*-GBM, in the range $10^{52} < E_{iso} < 10^{54}$ erg. In the opposite case, i.e. for longer binary periods, a more M-NS originates from the SN hypercritical accretion process (Wang et al. 2019). These BdHNe II are characterized by $10^{50} < E_{iso} < 10^{52}$ erg (Ruffini et al. 2016b). The BdHNe III are characterized by binaries with even longer periods, so with more widely separated components, leading to an even weaker energy emission with $10^{48} < E_{iso} < 10^{50}$ erg.

(iii) We make use of recent theoretical results in the study of the hypercritical accretion of the SN ejecta both on the companion NS

and the νNS (see e.g. Becerra et al. 2016, 2019; Ruffini et al. 2016b, 2018a; Rueda et al. 2020). We rely on the three-dimensional (3D) simulations performed with a new smoothed particle hydrodynamics (SPH) code developed in collaboration with Los Alamos National laboratory (see e.g. Becerra et al. 2019, and reference therein). We here give special attention to this procedure in order to reconstruct the morphology of the BdHNe, which has a strong dependence on the viewing angle as a result of the binary nature of the progenitor. We use the observations of the GeV emission observed by *Fermi*-LAT present only in *some* BdHN to infer their morphology and visualize its nature by SPH simulations (see Sections 6 and 7 and Fig. 4).

### 1.6 The role of the binary progenitor in the SN associated with long GRBs

Contrary to the case of S-GRBs, the necessity of a binary progenitor in long GRBs did not arise from the very beginning, and possibly the most important observational piece of evidence of this need can be identified in the temporal and spatial coincidence of GRB 980425 (Pian et al. 2000) and SN 1998bw (Galama et al. 1998), and the subsequent systematic spectroscopic analysis of additional GRB-SN associations (see Cano et al. 2017, for a review).

There are two key observational aspects of the SNe associated with GRBs pointing to a relevant role of binary interactions: (1) they are of type Ic, namely both hydrogen and helium lack in their spectra, and (2) the spectral lines are broad-lined implying their ejecta expand at very high expansion velocities of the order of 10^4 km s^{-1}, implying kinetic energies of up to 10^{52} erg, the reason for which they have been dubbed HN (Cano et al. 2017).

The first feature, namely that these SNe are of type IC implies that they possibly originate from helium stars, CO_{core}, or Wolf–Raye stars that have rid of their outermost layers (see e.g. Smith et al. 2011). Indeed, it has been recognized that a binary companion would most efficiently help in stripping off the pre-SN star outermost layers by tidal effects, multiple mass-transfer, and common-envelope episodes (see e.g. Nomoto & Hashimoto 1988; Iwamoto et al. 1994; Fryer et al. 2007; Yoon, Woosley & Langer 2010; Smith et al. 2011).

The second feature, namely the observed high-expansion velocities of the SN ejecta, is more delicate and less straightforward to account for in theoretical models. In the BdHN model, numerical simulations in Ruffini et al. (2018a) have shown that the explosion of the GRB within the SN might transfer to it sufficient energy and momentum to convert an initial ordinary SN into an HN. Therefore, broad-lined SNe or HNe in the BdHN model does not necessarily need to be born as such, instead they can be the outcome of the GRB feedback into the SN (see also Becerra et al. 2019). Evidence of such a transition from an SN into an HN in a BdHN has been observationally identified in GRB 151027A (see Ruffini et al. 2018c, for details).

In addition, binary interactions may enforce corotation of the pre-SN star (i.e. the CO_{core}) thereby spinning it up to high rotation rates. For BdHN I, this implies a rotation period of the CO_{core} of the order of minutes, so a rotational energy $\sim 10^{50}$ erg (Wang et al. 2019). Of course, this cannot explain directly an observed kinetic energy of 10^{52} erg. The core collapse of the iron core of this rotating CO_{core}, by angular momentum conservation, implies the birth of a millisecond period νNS, which may well power the SN by injecting into it energies of the order of 10^{52} erg (see Wang et al. 2019; Rueda et al. 2020, for more details). It may also happen that binary interactions spin-up the CO_{core} beyond corotation bringing it to even to higher rotation rates ~ 1 rad s^{-1} (see e.g. Nakamura et al. 2014;
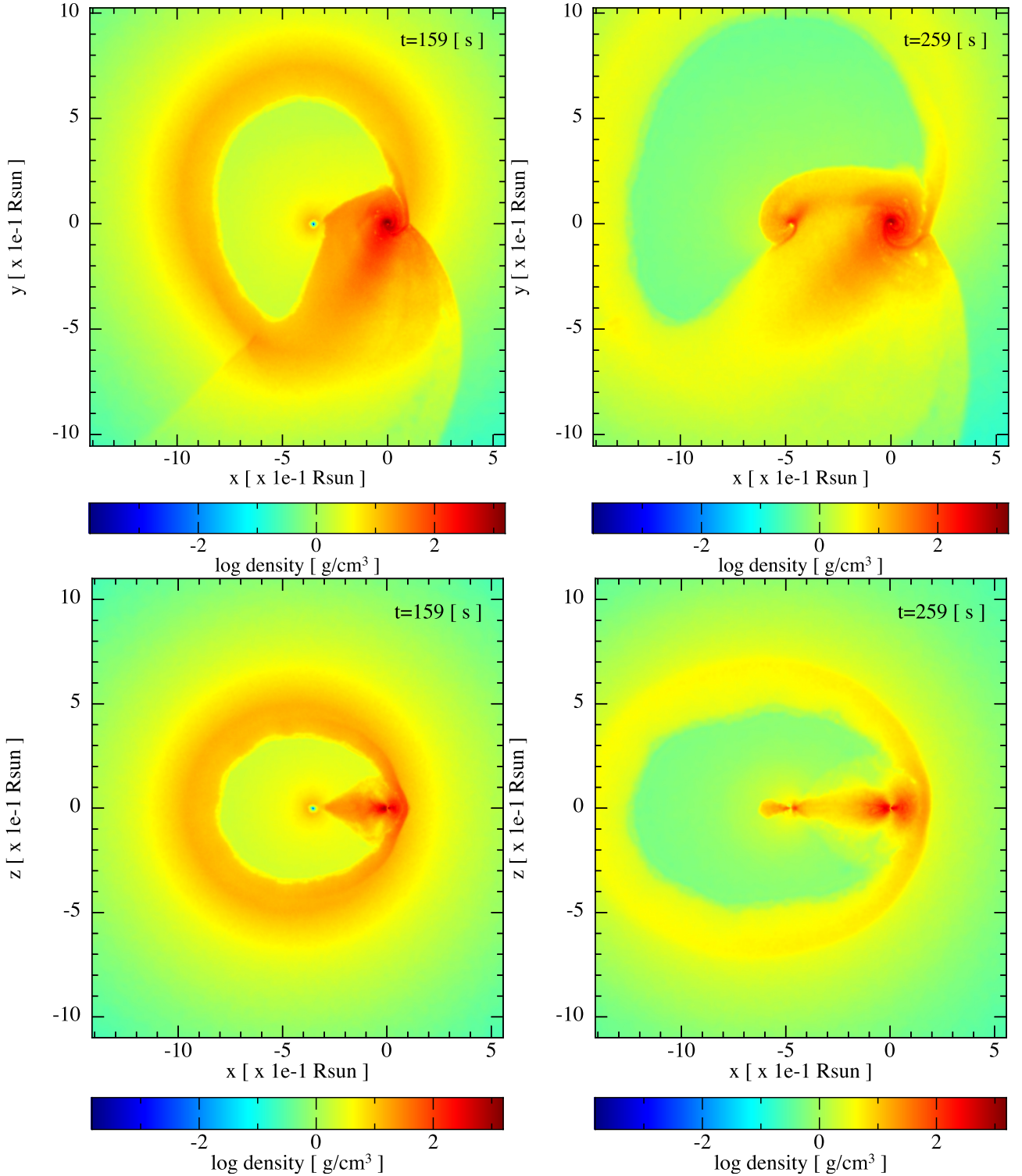
Figure 4. An SPH simulation from Becerra et al. (2019) of the exploding CO-star as the SN in the presence of a companion NS: Model '25m1p08E' (see table 2 therein). The CO-star is obtained from the evolution of a 25 $M_\odot$ zero-age main-sequence (ZAMS) progenitor that leads to a pre-SN CO-star mass $M_{CO} = 6.85\,M_\odot$. The initial mass of the νNS (formed at the centre of the SN) is 1.85 $M_\odot$ and the one of the NS companion is $M_{NS} = 2\,M_\odot$. The initial orbital period is 4.8 min. The upper panels show the mass density on the binary equatorial plane and the lower ones correspond to the plane orthogonal to it, at two selected times from the SN explosion ($t = 0$ of the simulation), 159 and 259 s. The reference system is rotated and translated so that the x-axis is along the line that joins the νNS and the NS, and the axis origin $(0, 0)$ is located at the NS position. For this simulation, the NS collapses reaching the secular axisymmetric instability point with a mass 2.26 $M_\odot$ and angular momentum $1.24 G M_\odot^2/c$, while the νNS is stable with mass and angular momentum, respectively, 2.04 $M_\odot$ and $1.24 G M_\odot^2/c$. Up to the final simulation time, the binary system kept bound although the binary orbit widens, reaching an orbital period of 16.5 min and an eccentricity of $\epsilon = 0.6$. The collapse of the NS to the newly formed BH, characteristic of a BdHN I, occurs at $t = 21.6$ min.

Gilkis 2018; Fujisawa et al. 2019), which would imply a much larger rotational energy of a few 10^{52} erg, ready to be used in the SN event.

There is increasing observational evidence on the high energetics of up to 10^{52} erg and the complex nature of the SN from the X- and gamma-ray precursors to the prompt radiation in long GRBs (see e.g. Wang et al. 2019). In order to account for such a complexity, we have dubbed these early phases of the BdHN as '*SN-rise*' (Li et al. 2019). The *SN-rise* triggers the entire BdHN, so it includes the SN explosion as well as the feedback of the hypercritical accretion on to the νNS and on to the binary companion NS. We dedicate Section 3 to their analysis giving examples in the case of BdHN I and II.

We can conclude that the binary progenitor of the BdHN model provides a natural explanation of the observational features of the SN associated with long GRBs. Having said this, it is now appropriate to discuss the formation of the CO_{core}–NS binary progenitors of the BdHN from the stellar evolution viewpoint.

It is well known from the stellar evolution theory and observations that massive binaries might evolve to form binaries composed of compact objects, e.g. WD–WD, NS–WD, NS–NS and NS–BH. Leaving aside specific technical details, traditional evolutionary paths lead the compact remnant of the more massive star, after undergoing SN, to common-envelope phase with the companion, and after the collapse of the companion star leading to the second SN, the system forms a compact-object binary provided it keeps bound (Fryer, Woosley & Hartmann 1999; Dominik et al. 2012; Postnov & Yungelson 2014). It is very interesting that alternative evolutionary scenarios have been recently proposed in the X-ray binary and SN community leading to the so-called *ultrastripped* binaries used to explain NS–NS and low-luminosity SNe (see e.g. Tauris et al. 2013; Tauris, Langer & Podsiadlowski 2015, for details). The binary in these cases, after first SN, experiences multiple mass-transfer phases leading to the expulsion of the hydrogen and helium shells of the secondary. As proposed in Becerra et al. (2015) and Fryer et al. (2015), these evolutionary scenarios are a plausible path to form CO_{core}–NS binary progenitors of BdHN.

From the above descends the question of whether such a population of binaries might or not include the progenitors of the BdHN. The orbital periods of the binary at the end of the evolution in these population synthesis codes are 50–5000 h (Tauris et al. 2013). They have been used as a main channel to form NS–NS, but the formation of NS–BH binaries, which are the final outcome left by BdHN I, have not been up to now considered in population synthesis numerical codes. One of the main reasons for this is that the physical processes involved in a BdHN I, occurring when shorter orbital periods of the order of minutes are allowed, lead to BH formation and they have not accounted for yet in these numerical codes. This is certainly a major research that deserves to be pursued in the near future.

We refer to Fryer et al. (2015) for additional details on the following estimation of the BdHN progenitor population. Ultrastripped binaries are expected to be 0.1–1 per cent of the total SN (Tauris et al. 2013), which is estimated to be 2×10^4 Gpc^{-3} yr^{-1} (see e.g. Guetta & Della Valle 2007). The population densities of BdHN II/III and BdHN I have been estimated to be $\sim$100 and $\sim$1 Gpc^{-3} yr^{-1}, respectively (Ruffini et al. 2016b). The above numbers imply, for instance, that BdHN I would comprise of only the 0.5 per cent of the ultrastripped binaries. These estimates confirm, in passing, the rareness of the GRB phenomenon.

Since 2018, our research on BdHN has acquired a different status by promoting technical progress in the visualization and in the data analysis, as well as in the introduction of new theoretical paradigms and identification of new astrophysical regimes that we further extend in this article. We start with a specific example of BdHN simulation.

1.7 A specific BdHN I SPH simulation

In Fig. 4, we show the results of a specific SPH simulation of a BdHN I from Becerra et al. (2019). It represents the implosion of a CO_{core} of 6.85 M$_\odot$ giving origin to the explosion of an SN in presence of a binary companion NS of $M_{NS} = 2$ M$_\odot$. An additional NS of 1.85 M$_\odot$ originates from the collapse of the Fe-core within the CO_{core} (the green dot at the centre of the SN in the two left figures). We indicate as νNS this newborn neutron star, in order to differentiate it from the binary companion NS. The two upper panels correspond to the mass density in the binary equatorial plane of the binary progenitor, which we label for short as 'seen in the orbital plane'. The lower panels correspond to viewing in a plane orthogonal to the equatorial plane of the binary progenitor, indicated for short as 'seen from the top'. This figure well summarizes the central role of the SN in triggering the BDHN1 phenomenon: by first creating the νNS and the accreting SN ejecta both on the νNS and the binary NS companion. The sequence of the accretion process is followed in these Figs 159 s and 259 s. Following the hypercritical accretion process, the νNS reaches a mass and angular momentum, 2.04 M$_\odot$ and $1.24 GM_\odot^2/c$, respectively. Up to the final simulation time. Similarly, the binary NS companion collapses reaching the secular axisymmetric instability point with a mass of 2.26 M$_\odot$ and angular momentum $1.24 GM_\odot^2/c$ at $t = 21.6$ min. In this model, the initial binary period of the circular orbit is 4.8 min. The binary orbit then widens, reaching an orbital period of 16.5 min and an eccentricity of $\epsilon = 0.6$. We are going to give specific examples in selected GRBs of this process in Section 10 with the determination of the mass and spin of the newborn BH. This figure is also essential in emphasizing the implications of the different viewing angles implied by the binary nature of the progenitors, which have been also neglected in the traditional approach.

We further exemplify, in the next two sections, the large amount of results inferred on the BdHN nature utilizing the two above viewing angles.

1.8 The upper limits on the Lorentz Γ factor and nature of the afterglow

The observations of BdHN I 'seen in the orbital plane' have been addressed in a series of articles based essentially on the X-ray observations made with the XRT detector in *Swift* (see e.g. Ruffini et al. 2018a, and references therein). They have been essential in identifying model-independent upper limits on the Lorenz Γ factors of the emission regions during the gamma-ray flare, the X-ray flares phase, the flare-plateau, and the early afterglow phases (the Nousek–Zhang phase), following the initial ultrarelativistic prompt radiation phase.

The traditional approach had shown that gamma-ray spikes in the prompt emission occur at $\sim 10^{15}$–10^{17} cm with Lorentz gamma factor $\Gamma \sim 10^2$–10^3 (e.g. Li 2020). Using a novel data analysis, we have shown that the time of occurrence, duration, luminosity, and total energy of the X-ray flares correlate with E_{iso}. A crucial feature has been identified in the observation of thermal emission in the X-ray flares that we have shown occurs at radii $\sim 10^{12}$ cm with $\Gamma \lesssim 4$. The upper limit of Lorentz factor, $\Gamma \lesssim 2$, has been there established in the analysis of the X-ray flares. Equally, an upper limit $\Gamma \lesssim 3$ has been set in the transition from a SN to an HN in GRB 151027A (Ruffini et al. 2018c). Finally, the limit $\Gamma \lesssim 2$ has been established in the thermal emission in the early part of the afterglow phase of GRB 130427A (Ruffini et al. 2018b).

The enormous kinetic energy of an ultrarelativistic blast wave needed in the traditional approach to explain the energy source of

the afterglow has been therefore superseded: the above mentioned stringent upper limits on the Γ factors exclude any ultrarelativistic motion.

The origin of the afterglow of long GRBs and these mildly relativistic processes have been successfully identified in the synchrotron emission produced by relativistic electrons in the SN ejecta, powered by the hypercritical accretion of the SN into the spinning νNS of 1.5 $M_\odot$ and its pulsar-like emission (Ruffini et al. 2018b; Wang et al. 2019; Rueda et al. 2020). From the amplitude of their decaying X-ray luminosities observed by *Swift*-XRT (Pisani et al. 2016), the spin of the νNS and the strength and structure of its magnetic field in specific BdHN I and II have recently been obtained (Rueda et al. 2020).

It is important that the synchrotron process occurring in the interaction of the SN ejecta with the νNS requires a much smaller energy to explain the nature of the afterglow in our present approach based on the hypercritical accretion from the SN on to the νNS (Wang et al. 2019; Rueda et al. 2020) than the ones purported in the ultrarelativistic blast waves.

1.9 The '*inner engine*' of BdHN I

The observations of the BdHN I 'seen from the top' are the main topic of this article. They lead to an identification of the morphology of BdHN I, to the origin of the MeV, GeV, and TeV emissions observed by the GBM and LAT instruments onboard the *Fermi* satellite, the *MAGIC* and the H.E.S.S telescopes, as well as a contribution to ultrahigh-energy cosmic rays (UHECRs) from GRBs (see e.g. Rueda & Ruffini 2020). Particularly important has been the recent identification of the physical process occurring in the '*inner engine*' originating from the GeV emission as 'seen from the top' in GRB 130427A, also confirmed in three additional BdHN I GRB 160509A, GRB 160625B, and GRB 190114C (Li et al. 2019; Ruffini et al. 2019c).

In these works:

(i) We have proposed that the *inner engine* of a BdHN I is composed of a Kerr BH in a non-stationary state, embedded in a uniform magnetic field B_0 aligned with the BH rotation axis, as modelled by the Papapetrou–Wald solution of the Einstein–Maxwell equations (Papapetrou 1966; Wald 1974), and surrounded by an extremely low density ionized plasma of 10^{-14} g cm^{-3}. Using GRB 130427A as a prototype, we have shown that this *inner engine* acts in a sequence of *elementary impulses* emitting '*blackholic quanta*' (Rueda & Ruffini 2020). The repetition time of the emission of each '*blackholic quantum*' of energy $\mathcal{E} \sim 10^{37}$ erg is $\sim 10^{-14}$ s at the beginning of the process. Then, it slowly increases with the time evolution. Electrons are accelerated to ultrarelativistic energy near the BH horizon and propagate along the polar axis, $\theta = 0$. They can reach energies of $\sim 10^{18}$ eV, and partially contribute to UHECRs. When propagating along $\theta \neq 0$ through the magnetic field B_0 they give rise to the synchrotron emission of GeV and TeV photons. The *inner engine* operates within a 'cavity' formed during the hypercritical accretion of the SN ejecta on to the NS binary companion, and during the BH formation (Ruffini, Melon Fuksman & Vereshchagin 2019b). This result is the first step towards identifying the BdHN I morphology, presented in this article.

(ii) It has been shown that the multiwavelength emissions corresponding to the above acceleration process leading to synchrotron radiation occur in a jet with a half-opening angle of $60°$ from the normal to the binary plane. The jetted emission occurs in selected energy bands in the MeV, GeV, TeV, and UHECR.

(iii) This result has been applied to GRB 130427A, and we here show that it applies generally to all BdHN I as a consequence of the novel morphology identified in this article.

(iv) We have evaluated the total GeV emission in GRB 130427A and identified its decaying luminosity in the GeV range with a power-law index of $\alpha_{\mathrm{GeV}} = -1.19 \pm 0.04$, using the first and the second *Fermi*-GRB catalogues (Ackermann et al. 2013; Ajello et al. 2019). In this article, we generalize this result to all BdHN I emitting GeV radiation.

1.10 On the measure of the BH mass and spin in BdHN I

For the first time, in Ruffini et al. (2019c) it was shown how to extract the rotational energy of a Kerr BH in an astrophysical system, using GRB 130427A as a prototype. This was made possible making use of the the mass–energy formula of the Kerr BH (Christodoulou 1970; Christodoulou & Ruffini 1971; Hawking 1971, 1972), given in equation (1a). There, it was shown how through the '*inner engine*' activity the energetics of the GeV emission could originate near the BH horizon and be explained using the extractable energy of the BH, keeping constant the BH *irreducible mass*. In turn, this has led to the first measure of the initial mass and spin of the BH at its moment of formation: $M = 2.3$ $M_\odot$, its spin, $\alpha = a/M = 0.47$. This article is dedicated to extend this classic result to all BdHN I, where sufficient GeV emission data are available. This same procedure will be soon extended to active galactic nuclei with BH masses up to 10^{10} $M_\odot$.

1.11 Structure of the article

We first give in Section 2 an outline of the nine GRB subclasses presented in Ruffini et al. (2016b), with a brief summary of their initial states (*in-state*), their final state (out-state), their energetics, and spectral properties in the gamma-rays both in the MeV and in the GeV emissions. We also recall the binary mergers that include the NS–NS binaries leading to the two classes of S-GRBs.

In Section 3, we summarize the previous results (Li et al. 2019) on the analysis of the SN-rise of BdHNe I and II obtained from *Fermi*-GBM, and present their relation with the X-ray afterglow observed by *Swift*-XRT.

In Section 4, following our previous works (Ruffini et al. 2018b; Wang et al. 2019; Rueda et al. 2020), we study properties of the X-ray afterglow of BdHNe and we determine the spin of the νNS in two BdHNe I, two BdHNe II, and one BdHN III system.

In Section 5, we analyse the properties of the GeV emission in BdHNe I updated following the second GRB catalogue presented by *Fermi*-LAT, which covers the first 10 yr of its operations, from 2008 August 4 to 2018 August 4 (Ajello et al. 2019). We address the 378 BdHNe I with known cosmological redshift; see the list of BdHNe I in Pisani et al. (2016), Ruffini et al. (2018a), and also the updated list in Appendix A. We then consider only the 54 BdHN I with the boresight angle of *Fermi*-LAT smaller than 75° at the trigger time. We give the details of the 25 BdHNe I with observed GeV radiation, out of the 54. For each of them, we list in Table 5 the cosmological redshift, the $E_{\mathrm{p,i}}$ of the spectrum, the $E_{\gamma,\mathrm{iso}}$ of the source, the *Fermi* GCN, the boresight angle, the E_{LAT}, the likelihood test statistic (TS), and some additional distinguishing properties. In Table 6 for the 29 BdHNe I, we then give the cosmological redshift, the $E_{\mathrm{p,i}}$ of the spectrum, the $E_{\gamma,\mathrm{iso}}$ of the source, the *Fermi* GCN, the boresight angle, and some distinguishing properties of the associated X-ray emissions.

In Section 6, we explain the nature of the these BdHNe in terms of a novel morphology of the binary system. The BdHN I have a conical

structure normal to the equatorial plane of the binary progenitor. When the observations are made with a viewing angle lying in the orbital plane of the binary progenitor then the GeV emission is not observable. In this case, only the gamma-ray flare, the X-ray flares, and the X-ray plateau remain observable. From the ratio $N_{LAT}/N_{tot} = 25/54$, we infer the presence in the BdHN I of a conical structure of approximately 60° around the normal to the plane of the binary progenitors. Within this cone all emissions are observable, namely the X-ray, the gamma-ray, the GeV and TEV emission, and UHECRs. For larger inclination angle as confirmed theoretically in Ruffini et al. (2018c, 2019c), the GeV radiation is not observable and only flaring activities are observed following the prompt radiation phase.

In Section 7, we show that this novel geometry is indeed present in the recent 3D SPH numerical simulations at the moment of BH formation in a BdHN (Becerra et al. 2019).

In Section 8, for each of the 25 BdHNe I, we provide the 0.1–10 GeV luminosity light curves as a function of the time in the rest frame of the source. We obtain a power-law fit $L_n = A_n t^{-1.19 \pm 0.04}$ erg s^{-1} and report the amplitude A_n and the luminosity at 10 s from the beginning of the prompt radiation, L_{10s}, with their associated uncertainties. We also provide a correlation between L_{10s} and $E_{\gamma,iso}$.

In Section 9, we determine the values of the mass and spin of the BH and the strength of the magnetic field surrounding the BH in the '*inner engine*' of the selected BdHNe I. We also show the process of hypercritical accretion of the SN on a companion NS gives in all cases origin to the newborn BH.

In Section 10, we confirm (1) the central role of the SN in giving rise to its hypercritical accretion on the νNS and the newly born BH, to the afterglow observed by SWIFT and to the high-energy GeV and TeV emission observed by Fermi-LAT, (2) that the MeV–GeV energetic range is explainable by extractable rotational energy of a Kerr BH operating n the '*inner engine*' and this result allows the determination of the initial mass and spin of the BH, and (3) the power-law evolution of the 0.1–100 GeV luminosity after the prompt phase arises from the slowing down rate of the BH spin, keeping constant the irreducible mass M_{irr} of the BH.

We finally proceed to the general conclusions in Section 11. Before proceeding, we indicate in Table 1 the alphabetic ordered list of acronyms used in this work.

2 SUBCLASSES OF GRBS AND DEFINITIONS OF BDHN

We address the specific role of the X-ray emission observed by the *Swift* satellite as well as the MeV–GeV radiation observed by the *Fermi* satellite in order to further characterize the nine subclasses of GRBs presented in Ruffini et al. (2016b) and updated in Ruffini et al. (2018a), Wang et al. (2019), and here further updated in Section 4 and Appendix A. In Table 2, we summarize for each GRB subclass their name, the number of observed sources with cosmological redshift, and their progenitors characterizing their 'in-state'.

In all cases, the GRB progenitors are binary systems composed of various combinations of CO$_{core}$, of NSs, of WDs, and of BHs. The 'out-state' of the corresponding mergers or accretion processes have been represented in fig. 7 in Ruffini et al. (2016b) where we also presented the interesting possibility that 'out-states' of the GRB subclasses can become the 'in-states' of new GRB subclasses. In particular, we indicate an example in which the 'out-state' of a BdHN I can become the 'in-state' of an S-GRB.

In this article, we focus only on long GRBs with BdHN progenitors (Ruffini et al. 2016b): binary systems composed of a CO$_{core}$,

exploding as SN Ic, and an NS binary companion. The presence of such an NS binary companion in close orbit can explain the removing of the outer layers of hydrogen and helium of the massive star leading to the CO$_{core}$ (see e.g. Ruffini et al. 2001; Rueda & Ruffini 2012; Fryer, Rueda & Ruffini 2014).

As noted in the introduction, when the CO$_{core}$ gravitationally collapses, it gives origin to an SN and its Fe core collapses to form a νNS. The entire dynamics and evolution of the BdHN is essentially based on these three different components and their interplay: the SN explosion (SN-rise), the νNS undergoing an overcritical accretion process of the SN ejecta, and the binary companion NS also undergoes an overcritical accretion process of the SN ejecta that monotonically increases the binary NS companion mass. In compact binary systems, this accretion causes the NS to reach its critical mass leading to the formation of a newborn BH (Becerra et al. 2015, 2016); see also Fig. 4.

We first address the SN hypercritical accretion on to the binary NS companion: the outcome is a strong function of the compactness of the binary system and its binary orbital period.

When the orbital period is as short as 5 min, the hypercritical accretion proceeds at higher rates and the companion NS reaches its critical mass leading to:

(i) the formation of a BH and consequently a formation of a new binary system composed of a BH and a νNS (Fryer et al. 2014);

(ii) the emission of a very energetic GRB in the range of $10^{52} \lesssim E_{iso} \lesssim 10^{54}$ erg and, peak energy in the range of 0.2 MeV < $E_{p,i}$ < 2 MeV lasting a few seconds known as the ultrarelativistic prompt emission phase (UPE);

(iii) the onset of the prolonged power-law GeV emission, triggered by the formation of the newborn BH, with a luminosity described in the rest frame of the source

$$L_{GeV} = A_{GeV} \left(\frac{t}{1\,s} \right)^{-\alpha_{GeV}}, \tag{2}$$

with $\alpha_{GeV} = 1.19 \pm 0.04$. One of the main results in this paper is to show that this radiation is present only in a subset of BdHN and the explanation of this result will lead to the determination of the conical BdHN morphology, see Section 8.

These systems have been indicated as BdHN I (Becerra et al. 2015, 2016; Ruffini et al. 2015b, 2016b, 2019c; Wang et al. 2019).

The first list of the BdHNe I was composed of 161 sources spanning 12 yr of *Swift*/XRT observation activity till 2015 presented in Pisani et al. (2016) which was further extended to 173 sources in Ruffini et al. (2018a) up through the end of 2016 which led to a total of 345 BdHNe I within 1997–2016 observed by other satellites like *Fermi* and *Konus*-WIND in addition to *Swift*. This list is further extended here to 378 BdHN I till 2018 December (see Appendix A and Table 2).

When the orbital period of the binary system is $\gtrsim 5$ min, the hypercritical accretion is not sufficient to trigger the collapse of the NS companion into a BH: therefore, no GeV emission can be produced nor be observed. Therefore, an M-NS is formed. In these systems, the observed peak energy is in the range 4 keV < $E_{p,i}$ < 300 keV and the isotropic energy is the range of $10^{48} \lesssim E_{iso} \lesssim 10^{52}$ erg, as observed by the *Fermi*-GBM. They have been indicated as X-ray flashes (XRF) in contrast with the more energetic BdHN I (Becerra et al. 2015, 2016; Ruffini et al. 2015b, 2016b). We here use for the XRFs the name BdHN II, according to Wang et al. (2019). A canonical example has been given in Wang et al. (2019); see Table 2.

BdHNe III have the same composition as BdHNe II, but the binary is further detached. No BH is formed and no GeV radiation

Table 2. Summary of the GRB subclasses. In addition to the subclass name, we report the number of GRBs for each subclass. We recall as well the 'in-state' representing the progenitors and the 'out-state' and the $E_{p,i}$ and $E_{\gamma,iso}$ for each subclass. The GeV emission is indicated in the last column: for long GRBs it appears only in BdHN I and BdHN IV (BH-SN) while, for short bursts, it appears only for S-GRBs. In all sources with GeV emission, it is $\gtrsim 10^{52}$ erg.

Class	Type	Number	In-state	Out-state	$E_{p,i}$ (MeV)	$E_{\gamma,iso}$ (erg)	$E_{iso,Gev}$ (erg)
Binary driven	I	378	CO star–NS	νNS–BH	~ 0.2–2	$\sim 10^{52}$–10^{54}	$\gtrsim 10^{52}$
hypernova	II	(49)	CO star–NS	νNS–NS	~ 0.01–0.2	$\sim 10^{50}$–10^{52}	–
(BdHN)	III	(19)	CO star–NS	νNS–NS	~ 0.01	$\sim 10^{48}$–10^{50}	–
	IV	0	CO star–NS	BH	–	$> 10^{54}$	$\gtrsim 10^{53}$
	I	18	NS–NS	MNS	~ 0.2–2	$\sim 10^{49}$–10^{52}	–
Binary	II	6	NS–NS	BH	~ 2–8	$\sim 10^{52}$–10^{53}	$\gtrsim 10^{52}$
merger	III	(1)	NS–WD	MNS	~ 0.2–2	$\sim 10^{49}$–10^{52}	–
(BM)	IV	(1)	WD–WD	NS/MWD	< 0.2	$< 10^{51}$	–
	V	(0)	NS–BH	Direct BH	$\gtrsim 2$	$> 10^{52}$	–

is produced nor observed. This subclass is characterized by binary systems widely separated and weaker energy emission with E_{iso} in the range of 10^{48}–10^{50} erg.

As we will see in Section 10, the most energetic BdHN I originate from extremely tight binary systems with the companion NS grazing the radius of the CO_{core}. It is therefore conceivable that in some systems the NS companion merges with the CO_{core} just prior to the SN explosion leading to the possible direct formation of a BH, a concept envisaged by Woosley (1993) in the failed SN scenario. We have left such a possibility opened in an additional BdHN IV family; see Table 2.

The hypercritical accretion of the SN ejecta on to the νNS leads to the pulsar-like emission that gives rise to the X-ray afterglow emission observed by *Swift* (Rueda et al. 2020). This is a property intrinsic to the nature of the model and shared by all BdHN subclasses. It is therefore natural to expect, as has been verified, that the luminosity of the X-ray afterglows of *all* long GRBs, in all BdHN subclasses, follow a common decaying power law of

$$L_X = A_X \left(\frac{t}{1\,s}\right)^{-\alpha_X}, \tag{3}$$

with $\alpha_X = 1.48 \pm 0.32$, including the SN-rise, when averaged over all BdHN I up to 10^6 s (Pisani et al. 2016). The different amplitudes, A_X, and power-law indices, α_X, of the X-ray afterglow luminosity can be used to determine the spin and magnetic field of the νNS (Wang et al. 2019; Rueda et al. 2020).

Before leaving this topic, we mention a few cases of X-ray afterglows in BdHN II and BdHN III. Each BdHN II and BdHN III must be also characterized by an X-ray afterglow originating from the accretion of the SN ejecta into the νNS. Their power-law index α_X coincides with the one of BdHN I, although the difference in the total angular momentum of the binary progenitors and its conservation leads necessarily to a smaller value of the amplitude A_X in equation (3), to a corresponding lower value of the νNS spin, and to a smaller value of the SN-rise; see Fig. 5.

In the rest of this article, we mainly examine the properties of BdHN I with special attention to:

(i) their SN-rise emission;

(ii) the power-law decay of the X-ray emission of the afterglow observed by *Swift*, measured in the cosmological rest frame of the source;

(iii) the corresponding GeV emission observed by *Fermi*-LAT, centring on the identification of the BdHN morphology to explain the absence of this emission in a subclass of BdHN I.

3 THE SN-RISE IN BDHN I AND BDHN II: FERMI OBSERVATION

The trigger of all BdHNe is represented by the gravitational collapse of the CO_{core} that gives origin to an SN and its Fe-core collapses to form a νNS. We have indicated the first appearance of the SN as the SN-rise. In BdHN I, the SN-rise is characterized by the presence of the thermal component in the *Fermi*-GBM data with isotropic energy of $\sim 10^{52}$ erg (see Fryer et al. 2014; Li et al. 2019; Ruffini et al. 2019a). In BdHN II, the SN-rise is weaker and has no thermal component in the *Fermi*-GBM data with energy of $\sim 10^{50}$ erg (see Li et al. 2019; Ruffini et al. 2019a; Wang et al. 2019; Fig. 6 and Table 3). In this article, we just recall the observation of the SN-rise in four BdHNe I: GRB 130427A, GRB 160509A, GRB 180720B, and GRB 190114C, as well as in two BdHNe II: GRB 180728A and GRB 190829A. In Fig. 6, we show the spectra of the SN-rise in the aforementioned sources and in Fig. 7 we show their corresponding luminosity.

## 4 THE AFTERGLOWS OF BDHN I, BDHN II, AND BDHN III: THE SWIFT OBSERVATIONS

Following the CO_{core} gravitational collapse and the appearance of the SN-rise, which characterizes all BdHN subclasses, the hypercritical accretion of the SN ejecta on to the νNS and the magnetic field of the νNS leads to the pulsar-like emission powering the X-ray afterglow observed by the *Swift* satellite (Rueda et al. 2020).

We present four afterglows of BdHN I (Fig. 7), two afterglows of BdHNe II, and one afterglow of BdHNe III (Fig. 5). In each case, we also reproduce the SN-rise presented in the previous section (see Figs 5 and 7).

The BdHN I in GRB 130427A, GRB 190114C, GRB 180720B, and GRB 160509A follow a decaying luminosity consistent with equation (3) (see Fig. 7):

(i) GRB 130427A with amplitude $(3.65 \pm 0.63) \times 10^{52}$ erg s^{-1} and power-law index $\alpha_X = 1.24 \pm 0.02$.

(ii) GRB 160509A with amplitude $(22.68 \pm 24.00) \times 10^{52}$ erg s^{-1} and power-law index $\alpha_X = 1.22 \pm 0.09$.

(iii) GRB 180720B with amplitude $(112.67 \pm 93.89) \times 10^{52}$ erg s^{-1} and power-law index $\alpha_X = 1.43 \pm 0.07$.

(iv) GRB 190114C with amplitude $(5.14 \pm 2.03) \times 10^{52}$ erg s^{-1} and power-law index $\alpha_X = 1.37 \pm 0.05$.

The BdHNe II in GRB 180728A and GRB 190829A follow a decaying luminosity consistent with equation (3) (see Wang et al. 2019; Figs 5a and b):
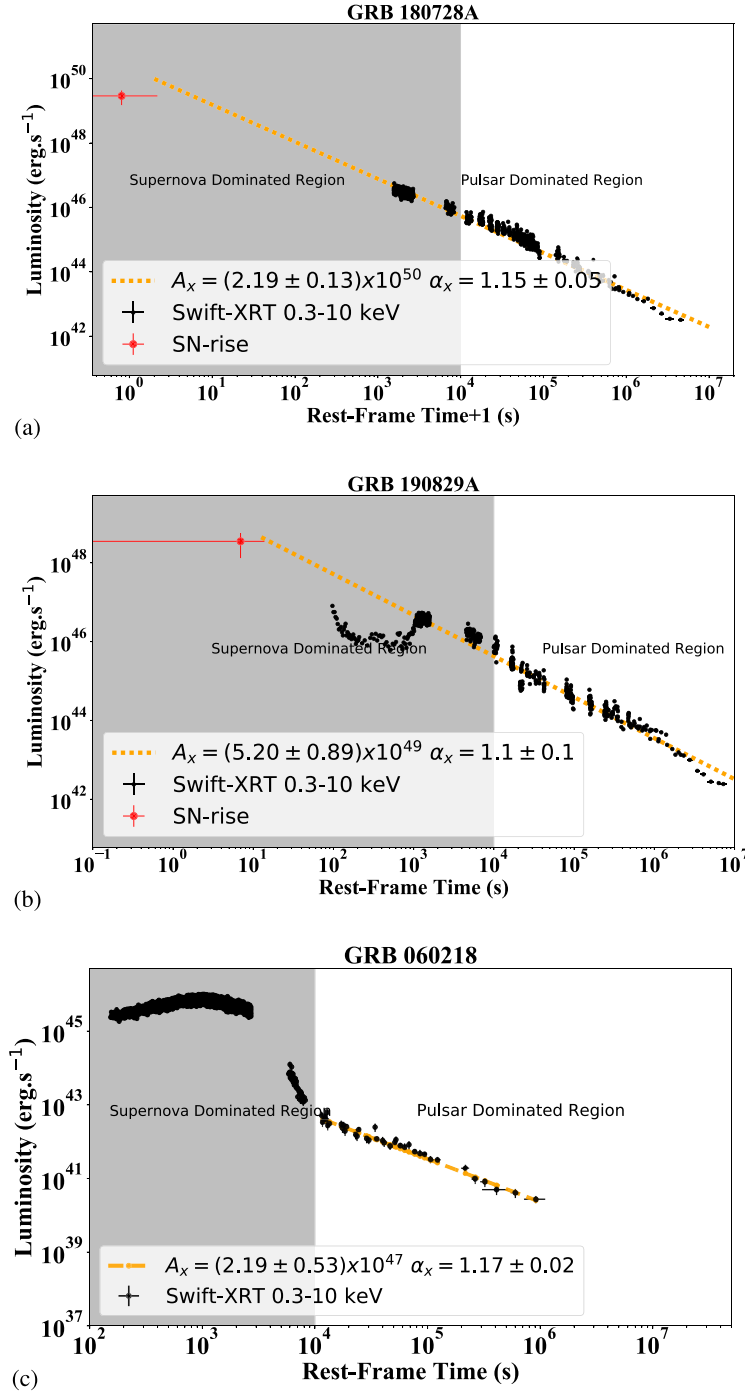
Figure 5. The X-ray afterglow luminosity observed by *Swift*-XRT that follow a decaying power law: (a) GRB 180728A (BdHN II) with amplitude $(2.19 \pm 0.13) \times 10^{50}$ erg s^{-1} and power-law index $\alpha_X = 1.15 \pm 0.05$. (b) GRB 190829A (BdHN II) with amplitude $(5.20 \pm 0.89) \times 10^{49}$ erg s^{-1} and power-law index $\alpha_X = 1.1 \pm 0.1$. (c) GRB 060218 (BdHN III) with amplitude $(2.19 \pm 0.53) \times 10^{47}$ erg s^{-1} and power-law index $\alpha_X = 1.17 \pm 0.02$. The fallback material of the SN on the νNS produce this X-ray afterglow emission (Rueda et al. 2020). In Section 4.1, we report the result of the simultaneous fit of the X-ray afterglow of all types of BdHN in order to find the universal power-law index. As shown in Ruffini et al. (2018a, c), until $\sim 10^4$ s the gamma/X-ray afterglow is mainly produced by the SN kinetic energy (*SN dominated region*) and its interaction with the magnetic field of the νNS. After 10^4 s, as shown by Ruffini et al. (2018b), the role of νNS becomes prominent (*pulsar dominated region*).

(i) GRB 180728A with amplitude $(2.19 \pm 0.13) \times 10^{50}$ erg s^{-1} and power-law index $\alpha_X = 1.15 \pm 0.05$.

(ii) GRB 190829A with amplitude $(5.20 \pm 0.89) \times 10^{49}$ erg s^{-1} and power-law index $\alpha_X = 1.1 \pm 0.1$.

As an example of the X-ray afterglow luminosity of a BdHN III, we indicate the case of GRB 060218 where the X-ray luminosity, as in the case of BdHNe I and II, follows a decaying power-law consistent with equation (3), with an amplitude $(2.19 \pm 0.53) \times 10^{47}$ erg s^{-1}
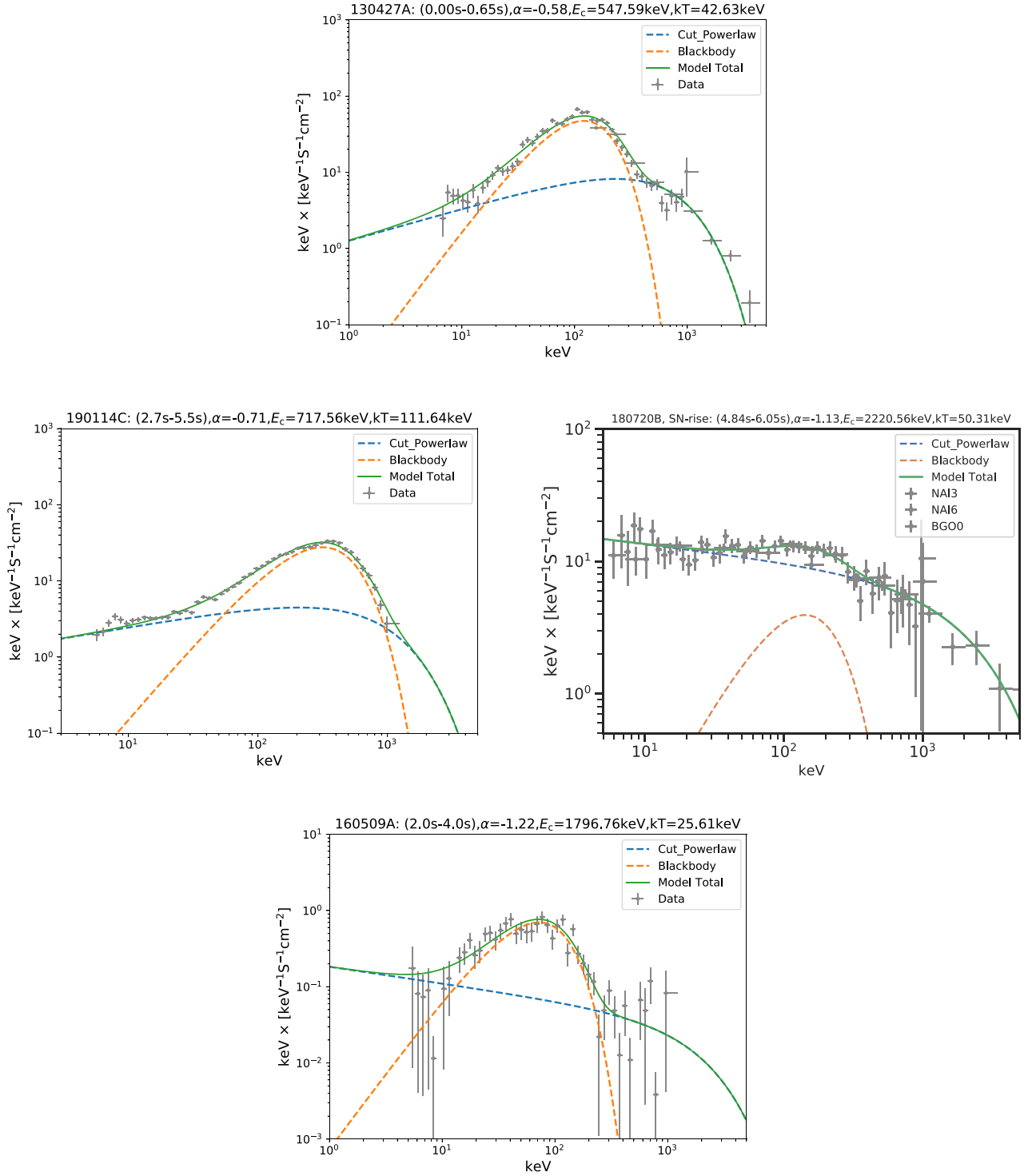
Figure 6. The spectrum of the SN-rise of GRB 160509A as observed by *Fermi*-GBM in the energy range of 8–900 keV. Upper left: SN-rise spectrum of BdHN I 130427A, well fitted by a CPL + BB model, from 0 to 0.65s ($t_{rf} \simeq 0.49s$); the spectral index α is -0.58, cut-off energy E_c is 547.59 keV, and the BB temperature is 42.63 keV in the observer's frame. Upper right: The spectra of SN-rise of BdHN I 190114C corresponding to $t = 1.12$ s ($t_{rf} = 0.79s$) to $t = 1.68$ s ($t_{rf} = 1.18s$), which is best fit by a CPL + BB model, with a low-energy photon index α of -0.71, and a peak energy E_c of 524.7 keV, and a BB temperature 18.42 keV. Time is reported in both the observer's frame and the rest frame. Spectral parameters of the best fit are presented in the observer's frame. Lower left: SN-rise spectrum of BdHN I 180720B, well fitted by a CPL + BB model, from 4.84 to 6.05 s ($t_{rf} \simeq 0.s$); the spectral index α is -1.13, cut-off energy E_c is 2220.569 keV, and the BB temperature is 50.31 keV in the observer's frame. Lower right: SN-rise spectrum of BdHN I 160509A, well fitted by a CPL + BB model, from 2.0 to 4.0 s ($t_{rf} \simeq 0.s$); the spectral index α is $-1.22.$, cutoff energy E_c is 1796.76 keV, and the BB temperature is 25.66 keV in the observer's frame.

Table 3. The properties of the SN-rise in BdHN I: GRB 190114C, GRB 130427A, GRB 160509A, and GRB 160625B; and the properties of the SN-rise in BdHN II: GRB 180728A.

GRB	$t_1 - t_2$ (s) (Observation)	Duration (s) (Rest)	Flux (erg cm^{-2} s^{-1})	E_{sh} (10^{52} erg) (SN-rise)	E_{iso} (erg) (Total)	Temperature (keV) (Rest)	Redshift	Reference (For SN-rise)
190114C	1.12–1.68	0.39	$1.06^{+0.20}_{-0.20}(10^{-4})$	$2.82^{+0.13}_{-0.13}$	$(2.48 \pm 0.20) \times 10^{53}$	$27.4^{+45.4}_{-25.6}$	0.424	Melandri et al. (2019)
130427A	0.0–0.65	0.49	$2.14^{+0.28}_{-0.26}(10^{-5})$	$0.65^{+0.17}_{-0.17}$	$\sim 1.40 \times 10^{54}$	$44.9^{+1.5}_{-1.5}$	0.3399	Xu et al. (2013)
160509A	2.0–4.0	0.92	$1.82^{+1.23}_{-0.76}(10^{-6})$	$1.47^{+0.6}_{-0.6}$	$\sim 1.06 \times 10^{54}$	$25.6^{+4.8}_{-4.7}$	1.17	Tam et al. (2017)
160625B	0–2.0	0.83	$6.8^{+1.6}_{-1.6}(10^{-7})$	$1.09^{+0.2}_{-0.2}$	$\sim 3.00 \times 10^{54}$	$36.8^{+1.9}_{-1.9}$	1.406	This paper
180728A	−1.57 to 1.18	0.83	$4.82^{+1.16}_{-0.82}(10^{-8})$	$7.98^{+1.92}_{-1.34} \times 10^{49}$	$2.76^{+0.11}_{-0.10} \times 10^{51}$	-	0.117	Izzo et al. (2018)
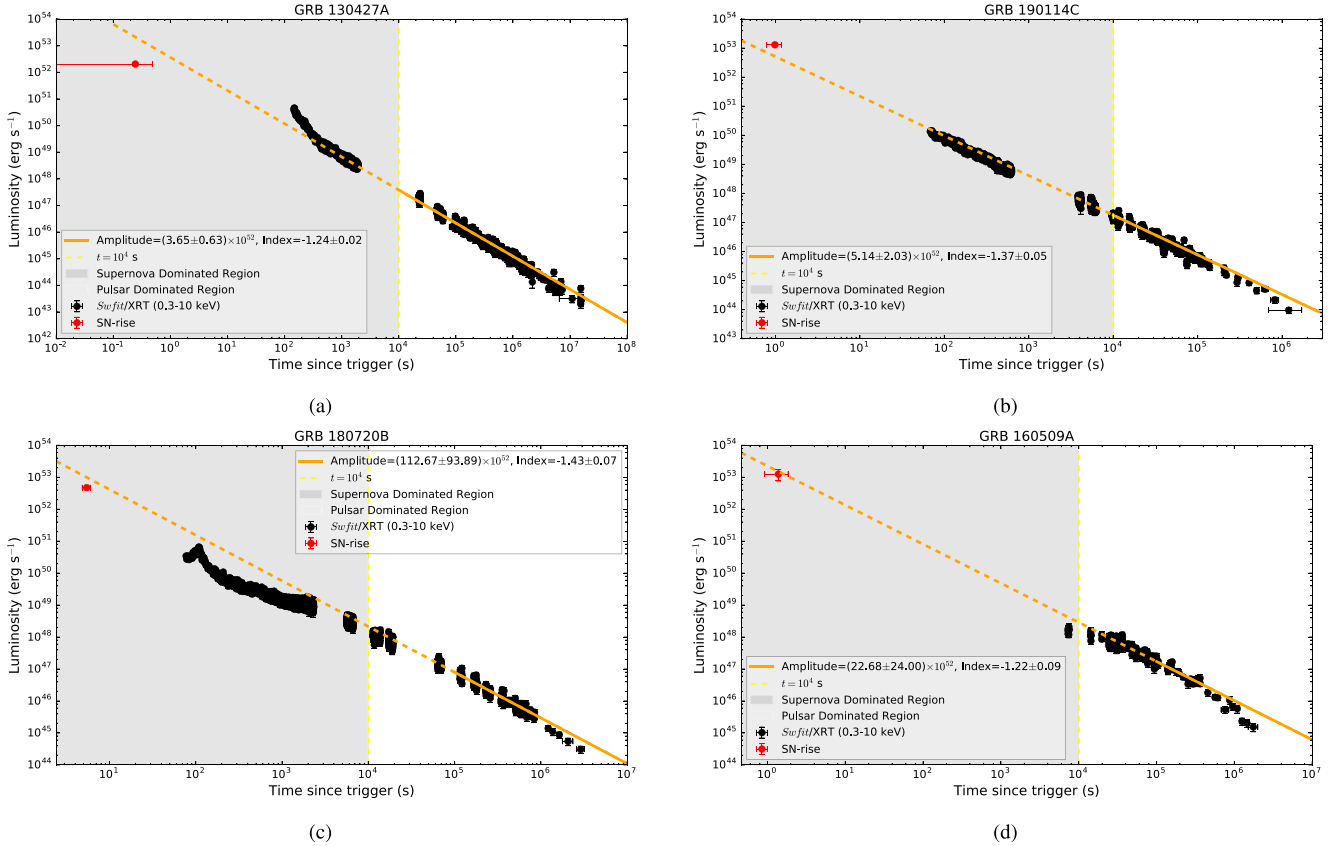
Figure 7. X-ray afterglow luminosities of four BdHNe I observed by *Swift*-XRT that follow a decaying power law: (a) GRB 130427A (BdHNe I) with amplitude $(3.65 \pm 0.63) \times 10^{52}$ erg s^{-1} and power-law index $\alpha_X = 1.24 \pm 0.02$. (b) GRB 190114C with amplitude $(5.14 \pm 2.03) \times 10^{52}$ erg s^{-1} and power-law index $\alpha_X = 1.37 \pm 0.05$. (c) GRB 180720B with amplitude $(112.67 \pm 93.89) \times 10^{52}$ erg s^{-1} and power-law index $\alpha_X = 1.43 \pm 0.07$. (d) GRB 160509A with amplitude $(22.68 \pm 24.00) \times 10^{52}$ erg s^{-1} and power-law index $\alpha_X = 1.22 \pm 0.09$. The red points show the luminosity of SN-rise in each BdHN. The fallback of material from the SN on to the νNS produces this X-ray afterglow emission (Rueda et al. 2020). As shown in Ruffini et al. (2018a, c), till $\sim 10^4$ s the gamma/X-ray afterglow is mainly produced by the SN kinetic energy (*SN dominated region*) and its interaction with the magnetic field of the νNS. After 10^4 s, as shown by Ruffini et al. (2018b), the role of νNS becomes prominent (*pulsar dominated region*).

and power-law index $\alpha_X = 1.17 \pm 0.02$. This is consistent with $\alpha_X = 1.2 \pm 0.1$ obtained by Campana et al. (2006; see Fig. 5c).

We can then reach the following general conclusions:

(i) The X-ray afterglow is present in all three BdHN subclasses: BdHN I, BdHN II, and BdHN III.

(ii) The X-ray afterglow is always present in *all* of the 378 BdHNe I (see Appendix A).

(iii) This result clearly indicates the spherical symmetry, or a very wide-angle emission of the X-ray afterglow.

4.1 The spin of the νNS

In Ruffini et al. (2018b), Rueda et al. (2020), and Wang et al. (2019), the bolometric luminosity contributing to the optical and X-ray bands by the νNS rotational energy loss by magnetic braking has been modelled for the emission at late times $t \gtrsim 10^4$ s of the 'Nousek–Zhang' (flare-plateau-afterglow, FPA phase). This allows the inference of the initial rotation period of the νNS as well as its magnetic field structure. The origin of the long GRB afterglows at this phase is the interaction between the SN ejecta and the spinning magnetized νNS and their synchrotron emission (Ruffini et al. 2018b).

Since the νNS is just born, it must be rapidly rotating and contains abundant rotational energy:

$$E_{\rm rot} = \frac{1}{2} I \Omega^2, \tag{4}$$

where I is the moment of inertia and $\Omega = 2\pi/P_{\nu\rm NS}$ is the angular velocity. For a νNS with a period of $P_{\nu\rm NS} = 1$ ms, $M = 1.4$ M$_\odot$, $R = 10$ km, the moment of inertia is $I \sim 10^{45}$ g cm^2. This leads to a total rotational energy of $E \sim 2 \times 10^{52}$ erg.

We assume that the rotational energy of the νNS provides the energy budget of the X-ray radiation via synchrotron emission of the electrons (Ruffini et al. 2018b):

$$E_{\rm rot} = E_{\rm X}. \tag{5}$$

This is reminiscent of the extraction of the BH rotational energy via synchrotron radiation of electrons radiating in the GeV energy band (Ruffini et al. 2019c).

Therefore, using the equation (4) and substituting the equation (3)

$$\frac{{\rm d}E_X}{{\rm d}t} = L_{\rm X}(t) = A_{\rm X} \left(\frac{t}{1{\rm s}}\right)^{-\alpha_{\rm x}} = -I\Omega\dot{\Omega}. \tag{6}$$

The best fit to the X-ray luminosity of equation (3), together with equation (6), allow an estimate of the spin of the νNS in *all* BdHNe, as well as their spin evolution (see Table 4 and Fig. 8).

In Table 4, we report the physical quantities of three BdHNe I, GRB 130427A, GRB 180720B, and GRB 190114C, together with two BdHNe II, GRB 180728A and GRB 190829A, as well as one BdHN III, GRB 060218; assuming a νNS of mass and radius, respectively, 1.4 M$_\odot$ and 10^6 cm. The νNS emission is not able to explain the emission of the 'Nousek–Zhang' phase at early times 10^2–10^4 s. As it is shown in Ruffini et al. (2018b, c), that emission is mainly powered by the mildly relativistic SN kinetic energy that we refer to as the *SN dominated region*. After 10^4 s, as shown by Ruffini et al. (2018b), the role of νNS becomes prominent, referred to as the *pulsar dominated region*.

The first main results of this paper are: (1) the first identification of the SN-rise, (2) the agreement of the extrapolated luminosity of the X-ray afterglow with the luminosity of the SN-rise, and (3) the measurement of the νNS period, leading to the power-law emission of the afterglow (see Fig. 7). The two process of the SN-rise energetics and the νNS dynamics appear to be strongly correlated.

5 BDHN I: THE FERMI-LAT OBSERVATIONS

5.1 BdHNe I observed by Fermi-LAT

We now address the 378 BdHNe I with known redshifts (see Pisani et al. 2016; Ruffini et al. 2018a; Appendix A): out of them, we are first interested in the 25 BdHNe I emitting GeV radiation and within the boresight angle of *Fermi*-LAT, i.e. $\theta < 75°$, at the time of the trigger, since exposure drops quickly for larger angles (Ajello et al. 2019). They have as well a TS value >25, which means the GeV photons are excluded at the 5σ level from background sources. We follow the first and second *Fermi* catalogues (Ackermann et al. 2013; Ajello et al. 2019) for the time-resolved likelihood spectral analysis. Therefore, we divide the data into logarithmic spaced bins and, if the TS value of each bin is smaller than 16, we merge the time bin with the next one and repeat the likelihood analysis. In Table 5, we indicate in the first column the name of the BdHNe I, in the second their measured redshift, we report in the third column the $E_{\rm p,i}$ obtained from the *Fermi* data, we estimate in the fourth column the

$E_{\gamma,\rm iso}$, which is itself larger than the 10^{52} erg. In the fifth column, the *Fermi* GCN numbers are shown. In the sixth column, the values of $E_{\rm LAT}$ are provided and finally we add the boresight angle of the LAT $\theta < 75°$ and the TS values of these GRBs observed by LAT.

5.2 BdHNe I without GeV emission and geometry of the BdHNe I

We now turn to an additional unexpected result obtained in the analysis of the BdHNe I subtended within the 75° of the *Fermi*-LAT boresight angle: the existence of 29 BdHNe I without observed GeV emission (see Table 6). Although the distribution of the boresight angle and redshift is analogous to the one of the 25 sources considered in Section 5, no GeV emission is observed.

Some BdHNe I of this group have been observed previously by *Swift* and have been identified as sources of (i) gamma and hard X-ray flares, (ii) soft X-ray flares, and of (iii) the extended thermal emission (see Ruffini et al. 2018a, for details). A particular example has been given by GRB 151027A in Nappo et al. (2017) and Ruffini et al. (2018c). There, we assumed that the viewing angle of these sources lies in the equatorial plane of the progenitor system (see Section 1 and Fig. 4). As we will show in this article, in none of these sources GeV radiation can be observed due to the new morphology discovered in the BdHNe I (see next section).

6 MORPHOLOGY OF BDHN I

We here assume that the 25 sources considered in Table 5, all emitting in the GeV have a viewing angle close to the normal of the plane. This assumption is confirmed in Ruffini et al. (2019c) where indeed the high-energy GeV–TeV radiations are emitted in direction close to the BH rotation axis.

The remaining 29 sources in Table 6 have a viewing angle in the equatorial plane of the binary progenitor and in that case only flaring activities in gamma and X-ray are observable, i.e. no GeV–TeV emission, as explicitly shown in Ruffini et al. (2018c, 2019c). This allows us to introduce a new morphology for the BdHNe I and predict specific observational properties.

We now look at the ratio between the number of GRBs with an observed GeV radiation, $N_{\rm LAT}$, and the total number of GRBs, $N_{\rm tot}$, both within the LAT 75° boresight angle. We assume that: (1) BdHNe I follow the same cosmological isotropic distribution of all GRBs first observed by the BATSE instrument onboard the CGRO satellite (see e.g. Meegan et al. 1992; Paciesas et al. 1999); (2) all orientations of the BdHNe I with respect to the LAT detector are equally probable; (3) the GeV emitting region is a two-side cone whose opening angle is the same for all sources. Under these assumptions, we can then estimate the half-opening angle of a single cone ϑ as

$$1 - \cos\vartheta = \frac{N_{\rm LAT}}{N_{\rm tot}}. \tag{7}$$

Our search in the LAT data[1] gives $N_{\rm LAT} = 25$ and $N_{\rm tot} = 54$, leading to $\vartheta \approx 60°$. Therefore, in BdHN I the GeV emission comes from a wide-angle emission, as it is schematically shown in Fig. 9. This is in agreement with theory of synchrotron radiation produced around the Kerr BH along the rotation axis (see details in Ruffini et al. 2019c).

Therefore, we have identified a *new* morphology of the BdHN I (see Figs 9 and 10). The identification of this morphology has been possible thanks to the analysis of the GeV emission in this paper, by

---

[1] https://fermi.gsfc.nasa.gov/ssc/observations/types/grbs/lat_grbs/table.php

Table 4. Observational properties of three BdHN I, GRB 130427A, GRB 180720B, and GRB 190114C together with two BdHNe II 180728A and 190829A as well as one BdHN III, GRB 060218 and inferred physical quantities of the νNS of the corresponding BdHN model that fits the GRB data. Column 1: GRB name; column 2: identified BdHN type; column 3: cosmological redshift (z); column 4: the isotropic energy released ($E_{\rm iso}$) in gamma-rays; column 5: νNS rotation period ($P_{\nu \rm NS}$) at 10^4 s, column 6: The isotropic energy of the X-ray afterglow ($E_{\rm X}$). We assume the NS mass of 1.4 M$_\odot$ and the NS radius of 10^6 cm for all these cases.

GRB	Type	Redshift	$E_{\rm iso}$ (erg)	$P_{\nu \rm NS}$@10^4 s (ms)	$E_{\rm X}$(after10^4 s) (erg)	$A_{\rm X}$ (erg s^{-1})	$\alpha_{\rm X}$
130427A	BdHN I	0.34	9.2×10^{53}	1.15	1.67×10^{52}	$(3.65 \pm 0.63) \times 10^{52}$	1.24 ± 0.02
180720B	BdHN I	0.654	6.8×10^{53}	0.66	4.99×10^{52}	$(112.67 \pm 93.89) \times 10^{52}$	1.43 ± 0.07
190114C	BdHN I	0.42	1.5×10^{53}	2.19	4.60×10^{51}	$(5.14 \pm 2.03) \times 10^{52}$	1.37 ± 0.05
180728A	BdHN II	0.117	2.3×10^{51}	7.74	3.68×10^{50}	$(2.19 \pm 0.13) \times 10^{50}$	1.15 ± 0.05
190829A	BdHN II	0.0785	2.2×10^{50}	10.31	2.07×10^{50}	$(5.20 \pm 0.89) \times 10^{49}$	1.10 ± 0.06
060218	BdHN III	0.033	5.4×10^{49}	285.81	2.69×10^{47}	$(2.19 \pm 0.53) \times 10^{47}$	1.17 ± 0.02
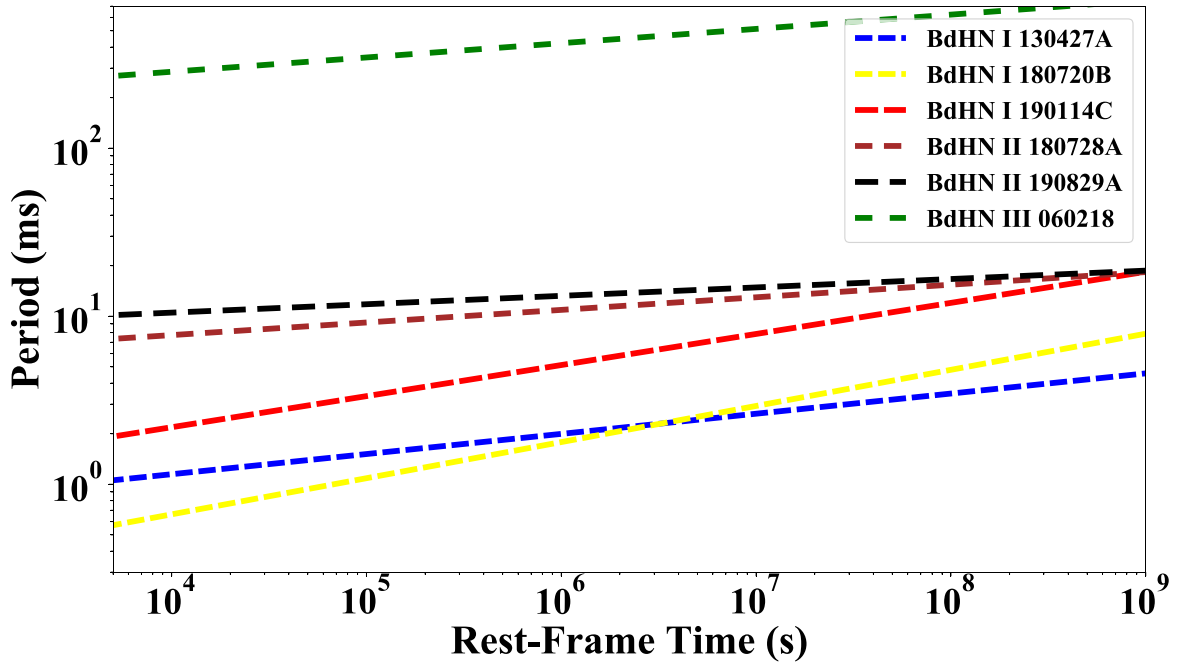
Figure 8. The evolution of the νNS period of six BdHNe, as a function of rest-frame time. The values of the νNS period at 10^4 s, namely in the pulsar dominated region of the afterglow are tabulated in Table 4. The trend of the νNS period indicates that the rotational energy is being released due to the radiation losses in the keV band revealing itself as the X-ray afterglow luminosity.

the soft and hard X-ray flares in Ruffini et al. (2018a), the extended thermal emission in Nappo et al. (2017), and Ruffini et al. (2018a) in GRB 151027A. In this identification, we have been guided by the large number of numerical simulations describing the accretion of the SN ejected material around the NS companion (see Figs 4 and 10, and its idealized representation in Fig. 9; see Becerra et al. 2016, 2019, for additional details).

What can be concluded from the above results is that in BdHNe I, the GeV emission is only detectable when the viewing angle is less than ≈60° from the normal to the plane and the BdHN I is 'seen from the top' (see the left-hand plot in Fig. 9). Whenever the viewing angle is within 60° from the orbital plane, no GeV emission is observed, though X-ray and gamma-ray flares are observed (see right-hand plot in Fig. 9).

Therefore, the second main result of this paper is the identification of the BdHN I morphology and its explanation within the BdHN I model.

7 SPH SIMULATION OF BDHNE I

The numerical simulations at the moment of BH formation in a BdHN I is presented in Becerra et al. (2016, 2019). 3D views of the density distribution at the moment of the BH formation in a BdHN I are shown Fig. 10. These plots correspond to the simulation of the SN ejecta expansion in the presence of the NS companion. The simulation is performed using an SPH code in which the SN ejecta material is evolved with N point-like particles, in the present case 16 million, with different masses and their motion is followed under the NS gravitational field. The orbital motion of the NS around the SN explosion centre is also taken into account as the NS star gravitational mass changes via the hypercritical accretion process. The latter was modelled independently estimating the accretion rate on to the NS via the Bondi–Hoyle formalism. For the initial conditions of the simulation, an homologous velocity distribution in free expansion was adopted and a power-law initial density profile of the SN matter was modelled by populating the inner layers with more particles (see

Table 5. Prompt and GeV emission of the 25 long GRBs inside the *Fermi*-LAT boresight angle and with GeV photons detected. The columns list: the source name, z, $E_{p,i}$, $E_{\gamma,iso}$, E_{LAT} in 0.1–10 GeV, the position of the source from the LAT boresight θ, the likelihood TS. The E_{LAT} includes only the energy in the observed time duration, which does not cover the whole GeV emission period, and is different for each GRB, so we put a symbol '$\gtrsim$' to indicate that the value is the lower limit.

GRB	z	$E_{p,i}$ (MeV)	$E_{\gamma,iso}$ (10^{52} erg)	Fermi GCN	E_{LAT} (10^{52} erg)	θ (deg)	TS
080916C	4.35	2.27 ± 0.13	407 ± 86	8246	230 ± 10	48.8	1450
090323A	3.57	2.9 ± 0.7	438 ± 53	9021	120 ± 20	57.2	150
090328A	0.736	1.13 ± 0.08	14.2 ± 1.4	9044	2.7 ± 0.4	64.6	107
090902B	1.822	2.19 ± 0.03	292.0 ± 29.2	9867	47 ± 2	50.8	1832
090926A	2.106	0.98 ± 0.01	228 ± 23	9934	149 ± 8	48.1	1983
091003A	0.897	0.92 ± 0.04	10.7 ± 1.8	9985	0.8 ± 0.3	12.3	108
091127	0.49	0.05 ± 0.01	0.81 ± 0.18	10204	0.03 ± 0.02	25.8	34
091208B	1.063	0.25 ± 0.04	2.10 ± 0.11	10266	$\gtrsim$ 0.41 ± 0	55.6	20
100414A	1.368	1.61 ± 0.07	55.0 ± 0.5	10594	7 ± 1	69	81
100728A	1.567	1.00 ± 0.45	72.5 ± 2.9	11006	0.9 ± 0.3	59.9	32
110731A	2.83	1.21 ± 0.04	49.5 ± 4.9	12221	15 ± 2	3.4	460
120624B	2.197	1.39 ± 0.35	347 ± 16	13377	22 ± 2	70.8	312
130427A	0.334	1.11 ± 0.01	92 ± 13	14473	8.6 ± 0.4	47.3	163
130518A	2.488	1.43 ± 0.38	193 ± 1	14675	15 ± 5	41.5	50
131108A	2.40	1.27 ± 0.05	51.20 ± 3.83	15464	37 ± 4	23.78	870
131231A	0.642	0.27 ± 0.01	21.50 ± 0.02	15640	1.6 ± 0.3	38	110
141028A	2.33	0.77 ± 0.05	76.2 ± 0.6	16969	9 ± 2	27.5	104.5
150314A	1.758	0.86 ± 0.01	70.10 ± 3.25	17576	1.8 ± 0.7	47.13	27.1
150403A	2.06	0.95 ± 0.04	87.30 ± 7.74	17667	1.1 ± 0.4	55.2	37
150514A	0.807	0.13 ± 0.01	1.14 ± 0.03	17816	0.06 ± 0.05	38.5	33.9
160509A	1.17	0.80 ± 0.02	84.5 ± 2.3	19403	10 ± 1	32	234
160625B	1.406	1.3 ± 0.1	337 ± 1	19581, 19604	17 ± 1	41.46	961.33
170214A	2.53	0.89 ± 0.04	392 ± 3	20675, 20686	53 ± 4	33.2	1571
170405A	3.51	1.20 ± 0.42	241.01 ± 52.02	20990, 20986	16 ± 7	52.0	56
180720B	0.654	1.06 ± 0.24	68.2 ± 2.2	22996, 23042	2.2 ± 0.2	49.1	975

Fryer et al. 2014; Becerra et al. 2016, 2019, for additional details). Figs 4 and 10 correspond to an initial binary system formed by a $2\,M_\odot$ NS and the CO_{core} obtained from a progenitor with $M_{ZAMS} = 30\,M_\odot$. When the CO_{core} collapses and explodes, it ejects $7.94\,M_\odot$ and leads a νNS of $1.5\,M_\odot$ at its centre. The initial binary period is about 5 min, corresponding to a binary separation of $\approx 1.5 \times 10^{10}$ cm.

The new morphology of the BdHNe I presented here and in the previous section leads to a difference in the observed energy spectra and time variability for sources with viewing angle in the plane, or normal to the orbital plane of the binary progenitor. We infer that our 25 BdHNe I, with viewing angles less than $\approx 60°$ from the normal to the orbital plane of the binary progenitor, 'seen from the top', have larger $E_{\gamma,iso}$ than the ones with a viewing angle lying in the plane of the binary system (see Tables 5 and 6). This explains the association/non-association of the GeV emission with bright GRBs often mentioned in the current literature (see Cenko et al. 2011; Racusin et al. 2011, and fig. 4 in Nava 2018).

An additional issue in the traditional approach (see e.g. Racusin et al. 2011; Beniamini et al. 2015, and sections 3 and 4 in Nava 2018) is also solvable: the sources that are seen with a viewing angle lying in the orbital plane have stronger flaring activities in the X-ray afterglow when compared to the 25 emitting in the GeV range. Therefore, the ratio between E_{iso} and the luminosity in the X-ray afterglow is systematically smaller than in the 25 with GeV emission. This offers a different explanation than the one presented in the traditional approach. However, all of these matters that have already been mentioned in Ruffini et al. (2018c) need a new operational definition of $E_{\gamma,iso}$, taking into due account the hard and soft X-ray flares and the extended thermal emission (see also Ruffini et al. 2019b).

Another important specific feature of the new morphology of BdHN I is the presence of the νNS formed at the centre of the exploding SN (see Fig. 4 and Becerra et al. 2016, 2019). We have shown that the νNS manifests itself through the synchrotron emission by relativistic electrons injected from it into the expanding magnetized SN ejecta, as well as through its pulsar emission that explain the early and late optical and X-ray afterglow, respectively, allowing the inference of the νNS rotation period (see Ruffini et al. 2018b). A smoking gun of this picture, namely the verification of the νNS activity following the above mechanism, both in XRFs (BdHNe II) and in BdHNe I, and the connection of the inferred rotation period of the νNS to the one of the CO-star and to the orbital period, from angular momentum conservation, has been explicitly shown in the GRB 180728A (BdHN II) and GRB 130427A (BdHN I) and GRB 190114C (BdHN I) (see Wang et al. 2019 for details).

8 THE LUMINOSITY POWER-LAW BEHAVIOUR IN BDHNE MEASURED IN THE REST FRAME

In the following, we fit simultaneously the luminosity light curves of all the 25 BdHNe with GeV emission expressed in their rest frame. We assume the same power-law decay index for all of them, but allow different amplitude values. This assumption is consistent with our model, moreover, it is a benefit for those GRBs with limited data that cannot be fitted solely.

Table 6. List of 29 BdHNe I inside the *Fermi*-LAT boresight angle and with no GeV photons detected: 29 BdHNe I with redshift taken from (Ruffini et al. 2016b) from 2008, when *Fermi* started to operate, till the end of 2016. All of them are within the boresight of *Fermi*-LAT, but no detected GeV photons. For each source the columns list: z, $E_{\gamma,\mathrm{iso}}$, E_p, GCN number, position of the source from LAT boresight θ, whether there was a detection by LAT, and additional information.

GRB	z	E_p (MeV)	$E_{\gamma,\mathrm{iso}}$ ($\times 10^{52}$ erg)	*Fermi* GCN	θ (deg)	GeV observed	Comments
081222	2.77	0.51 ± 0.03	27.4 ± 2.7	8715	50.0	No	
090424A	0.544	0.27 ± 0.04	4.07 ± 0.41	9230	71.0	No	
090516A	4.109	0.14 ± 0.03	99.6 ± 16.7	9415	20.0	No	Clear X-ray flare
100615A	1.398	0.21 ± 0.02	5.81 ± 0.11	10851	64.0	No	
100728B	2.106	0.32 ± 0.04	3.55 ± 0.36	11015	57.1	No	
110128A	2.339	0.46 ± 0.01	1.58 ± 0.21	11628	45.0	No	
111228A	0.716	0.060 ± 0.007	2.75 ± 0.28	12744	70.0	No	
120119A	1.728	0.52 ± 0.02	27.2 ± 3.6	12874	31.4	No	
120712A	4.175	0.64 ± 0.13	21.2 ± 2.1	13469	42.0	No	
120716A	2.486	0.4 ± 0.04	30.2 ± 3.0	13498	63.0	No	
120909A	3.93	0.87 ± 0.01	87 ± 10	13737	66.0	No	
130528A	1.250	0.27 ± 0.18	18.01 ± 2.28	14729	60.0	No	X-ray flare
130925A	0.347	0.14 ± 0.04	3.23 ± 0.37	15261	22.0	No	X-ray flare
131105A	1.686	0.55 ± 0.08	34.7 ± 1.2	15455	37.0	No	
140206A	2.73	1.1 ± 0.03	144.24 ± 19.20	15790	46.0	No	Clear X-ray flare
140213A	1.2076	0.176 ± 0.004	9.93 ± 0.15	15833	48.5	No	
140423A	3.26	0.53 ± 0.04	65.3 ± 3.3	16152	44.0	No	
140623A	1.92	1.02 ± 0.64	7.69 ± 0.68	16450	32.0	No	
140703A	4.13	0.91 ± 0.07	1.72 ± 0.09	16512	16.0	No	
140907A	1.21	0.25 ± 0.02	2.29 ± 0.08	16798	16.0	No	X-ray flare
141220A	1.3195	0.42 ± 0.02	2.44 ± 0.07	17205	47.0	No	
150301B	1.5169	0.45 ± 0.10	2.87 ± 0.42	17525	39.0	No	
150821A	0.755	0.57 ± 0.03	14.7 ± 1.1	18190	57.0	No	
151027A	0.81	0.62 ± 0.11	3.94 ± 1.33	18492	10.0	No	Clear X-ray flare
151111A	3.5	0.25 ± 0.04	3.43 ± 1.19	18582	50.0	No	X-ray flare observed
161014A	2.823	0.64 ± 0.06	10.1 ± 1.7	20051	69.0	No	
171222A	2.409	0.1 ± 0.01	20.73 ± 1.7	22272, 22277	43	No	
180703A	0.67	0.58 ± 0.05	3.15 ± 0.7	23889, 22896	44	No	
180728A	0.117	0.1 ± 0.02	3.15 ± 0.7	23055, 23067	35	No	
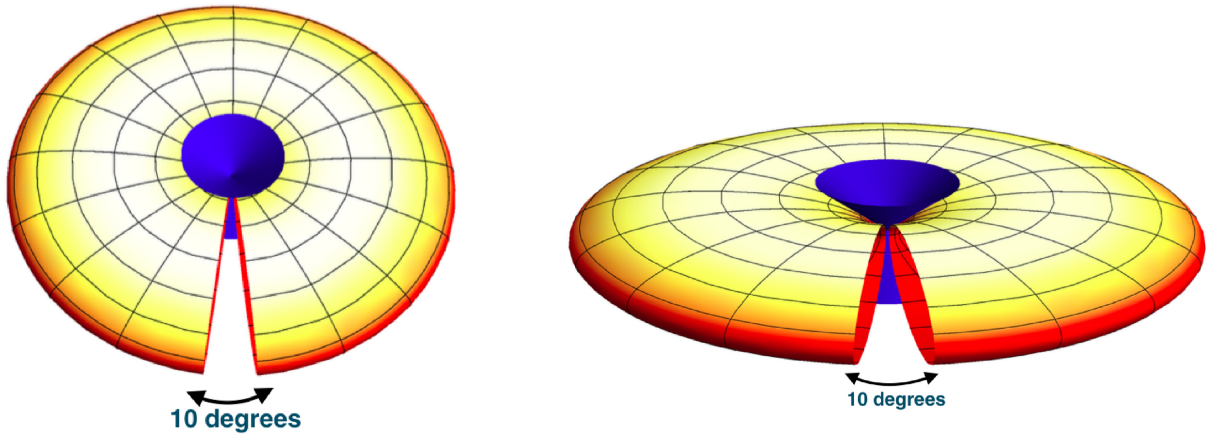
**Figure 9.** Schematic plot for showing the morphology of the BdHNe I. The GeV emission is detectable when the viewing angle is less than the $60°$ from the normal to the orbital plane. Left-hand panel is the situation in which the detectors can observe GeV and prompt emissions and the right-hand panel is the one for which GeV emission is not detectable and only gamma-ray and X-ray flares are detectable. The $10°$ cuts in both figures indicate the low-density region in Fig 10 through which the prompt radiation phase can be 'seen in the orbital plane'. The existence of such a $10°$ cut was first identified by the SPH simulation quoted in Becerra et al. (2016, 2019) and further confirmed in GRB 151027A (Ruffini et al. 2018c).

We limit our analysis of the light curves after the BdHN I prompt emission, when the GeV luminosity is already in the asymptotic power-law regime. We assume the power-law

$$L_n(t) = A_n t^{\alpha_{\mathrm{GeV}}},\tag{8}$$

describing the rest-frame 0.1–100 GeV isotropic luminosity light curve of nth BdHN I. In the simultaneous fitting, we perform the Levenberg–Marquardt method to perform the minimization (Gill & Wright 1981). The basic idea of fitting is to minimize the χ^2; when fitting one curve to one equation, the χ^2 is minimized. To fit N curves
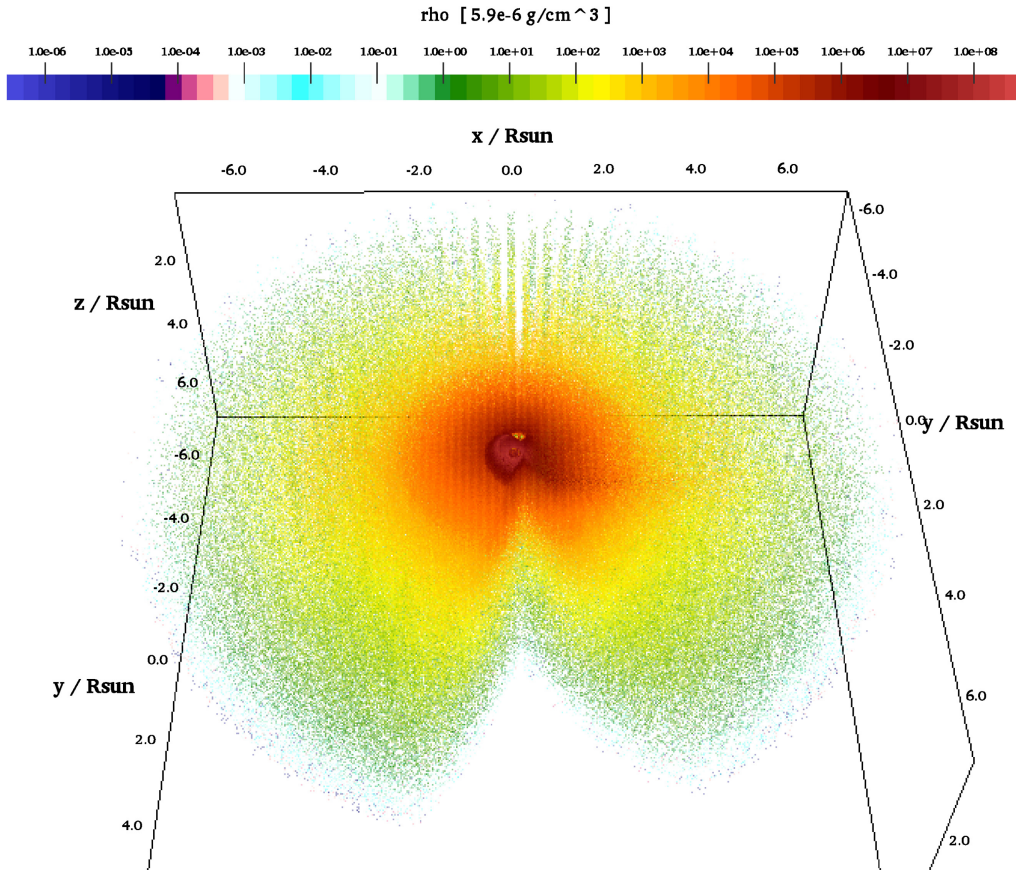
Figure 10. 3D, half-hemisphere views of the density distribution of the SN ejecta at the moment of BH formation in a BdHN I. The simulation is performed with an SPH code that follows the SN ejecta expansion under the influence of the NS companion gravitational field including the effects of the orbital motion and the changes in the NS gravitational mass by the hypercritical accretion process. The initial conditions of the SN ejecta are set as a homologous velocity distribution in free expansion and the mass distribution is modelled with 16 millions point-like particles (see Becerra et al. 2016, 2019, for additional details). The binary parameters of this simulation are: the NS companion has an initial mass of 2.0 $M_\odot$; the CO-star, obtained from a progenitor with ZAMS mass $M_{\rm ZAMS} = 30$ $M_\odot$, leads to a total ejecta mass of 7.94 $M_\odot$ and to a 1.5 $M_\odot$ νNS, the orbital period is $P \approx 5$ min (binary separation $a \approx 1.5 \times 10^{10}$ cm). The distribution of the ejecta is not axially symmetric; it is strongly influenced by the rotation of the system and accretion occurring in the binary component (see Fig. 4). Particularly relevant for the observations is the low-density region of $\approx 10°$ which allows the sources with viewing angle in the equatorial plane to detect the prompt radiation phase. This has been qualitatively indicated in Fig. 9. In these sources, only a fraction of approximately 10 per cent of the prompt radiation can be detectable, they are the only ones able to trigger the *Fermi*-GBM and the remaining 90 per cent will not have detectable prompt radiation (see Ruffini et al. 2018c). Figure is taken from Ruffini et al. (2018c) with the kind permission of the authors.

to N equations simultaneously, the sum of the χ^2 values should be minimized. The related equations are

$$\chi^2 = \sum_{n=1}^{N} \chi_n^2, \tag{9}$$

$$\chi_n^2 = \sum_{i=1}^{M} \frac{1}{\sigma_{ni}^2} (L_{ni} - L_n(t_{ni}, A_n, \alpha_{\rm GeV}))^2, \tag{10}$$

where n represents each BdHN I, i represents each data point in a given BdHN I, A_n is the amplitude of a power-law function for the nth BdHN I, and $\alpha_{\rm GeV}$ is the common power-law index shared for all the BdHNe I. Thus, for the nth BdHN I, at time t_{ni}, the observed luminosity is L_{ni}, and the predicted luminosity is $L_n(t_{ni}, A_n, \alpha)$. The value of χ^2 represents the difference between the best power-law fitting and all the observed data; it is a summation of individual χ_n^2, which represents the difference between the power-law fitting and the observed value of each GRB.

Out of 25 BdHNe I presented in Table 5, we perform the fitting for only 20 GRBs that have more than two data points in their luminosity light curves. Therefore, for the fitting of BdHNe I, there are 20 bursts and each one has its power-law function. Consequently, there are in

total 17 parameters, including 20 amplitudes, and 1 power-law index. The fitting gives a power-law index of $\alpha_{\rm GeV} = 1.19 \pm 0.04$, i.e.:

$$L_n = A_n \, t^{-1.19 \pm 0.04}, \tag{11}$$

which is plotted in Fig. 3 and the amplitudes of each GRB, A_n, with the uncertainty are shown in Table 7. This inferred power-law index is similar to the one obtained from fitting the GeV flux, $f_\nu(t)$ (see e.g. Kumar & Barniol Duran 2009; Panaitescu 2017), in which the power-law index is $\alpha_{\rm GeV} = 1.2 \pm 0.2$ and $\alpha_{\rm GeV} = 1.2 \pm 0.4$, respectively.

In our approach, we adopt an alternative interpretation of these power laws: instead of using the flux expressed in arrival time, we use the luminosity expressed in the rest frame of the source. Since the luminosity is proportional to the flux, i.e. $L = 4\pi d_L^2 (1 + z)^{\alpha_{\rm GeV} - 2} f_\nu$, where d_L is the luminosity distance, this similarity of the power-law index is not surprising. The advantage of using luminosity expressed in the rest frame of the source, instead of flux in arrival time, is that one can determine the intrinsic energy loss of the system that produces the GeV radiation, regardless of differences in the redshift

Table 7. Fitting parameters of the 0.1–10 GeV power-law luminosity when measured in the rest frame of 20 BdHNe with GeV emission: amplitude of the 0.1–10 GeV luminosity, A_n, and its uncertainty, the inferred 0.1–10 GeV luminosity at 10 s from the fitting and its uncertainty. The common power-law index is $\alpha_{\mathrm{GeV}} = 1.19 \pm 0.04$. Out of 25 BdHNe emitting GeV emission, we performed the fitting for 20 GRBs that have more than two data points in their luminosity light curves. GRBs 091127, 091208B, 130518A, 150314A, 150514A have only two data points in their GeV luminosity light curves.

BdHN	A_n (Amplitude)	Uncertainty of A_n	$L_{10\mathrm{s}}$	Uncertainty of L_{10s}
080916C	2.9×10^{53}	$^{+9.1}_{-7.4} \times 10^{52}$	1.88×10^{52}	$^{+1.1}_{-1.0} \times 10^{52}$
090323A	9.4×10^{53}	$^{+3.5}_{-2.9} \times 10^{53}$	6.04×10^{52}	$^{+3.8}_{-1.4} \times 10^{52}$
090328A	2.4×10^{52}	$^{+1.1}_{-0.7} \times 10^{52}$	1.5×10^{51}	$^{+1.0}_{-0.9} \times 10^{51}$
090902B	8.9×10^{52}	$^{+2.5}_{-2.0} \times 10^{52}$	5.7×10^{51}	$^{+3.3}_{-3.0} \times 10^{51}$
090926A	2.1×10^{53}	$^{+5.9}_{-4.8} \times 10^{52}$	1.4×10^{52}	$^{+7.9}_{-7.3} \times 10^{51}$
091003A	5.7×10^{51}	$^{+1.7}_{-1.5} \times 10^{51}$	3.7×10^{50}	$^{+2.1}_{-2.0} \times 10^{50}$
100414A	3.5×10^{52}	$^{+1.4}_{-1.1} \times 10^{52}$	2.3×10^{51}	$^{+1.4}_{-1.3} \times 10^{51}$
100728A	4.2×10^{51}	$^{+1.9}_{-1.5} \times 10^{51}$	2.7×10^{50}	$^{+1.9}_{-1.6} \times 10^{50}$
110731A	2.3×10^{52}	$^{+0.8}_{-0.5} \times 10^{52}$	1.8×10^{51}	$^{+0.9}_{-0.8} \times 10^{51}$
120624B	2.4×10^{53}	$^{+8.2}_{-6.2} \times 10^{52}$	1.6×10^{52}	$^{+9.6}_{-8.5} \times 10^{51}$
130427A	5.1×10^{52}	$^{+2.1}_{-2.0} \times 10^{51}$	3.3×10^{51}	$^{+1.3}_{-1.3} \times 10^{51}$
131108A	6.1×10^{52}	$^{+9.1}_{-8.9} \times 10^{51}$	3.9×10^{51}	$^{+2.0}_{-1.9} \times 10^{51}$
131231A	1.64×10^{52}	$^{+7.9}_{-5.4} \times 10^{51}$	1.1×10^{51}	$^{+7.3}_{-6.1} \times 10^{50}$
141028A	3.6×10^{52}	$^{+1.2}_{-1.1} \times 10^{52}$	2.3×10^{51}	$^{+1.4}_{-1.3} \times 10^{51}$
150403A	6.8×10^{51}	$^{+3.0}_{-2.3} \times 10^{51}$	4.3×10^{50}	$^{+2.9}_{-3.0} \times 10^{50}$
160509A	1.4×10^{52}	$^{+4.9}_{-3.8} \times 10^{51}$	8.9×10^{50}	$^{+5.4}_{-4.1} \times 10^{50}$
160625B	1.4×10^{53}	$^{+4.6}_{-3.4} \times 10^{52}$	8.7×10^{51}	$^{+5.2}_{-4.6} \times 10^{51}$
170214A	2.8×10^{53}	$^{+7.4}_{-5.9} \times 10^{52}$	1.8×10^{52}	$^{+1.0}_{-0.9} \times 10^{52}$
170405A	4.1×10^{52}	$^{+1.1}_{-1.0} \times 10^{52}$	2.5×10^{51}	$^{+1.5}_{-1.4} \times 10^{51}$
180720B	5.4×10^{52}	$^{+6.6}_{-6.1} \times 10^{51}$	3.5×10^{51}	$^{+2.2}_{-2.1} \times 10^{50}$

of the sources. This allows us following our recent understanding of the BdHN I 130427A (see Ruffini et al. 2019c, and references therein), to relate the GeV radiation to the slowing down of the BH spin (see Section 10).

After obtaining the best power-law parameters for the luminosity light curve for each BdHNe I, we check the correlation between the GeV luminosity at 10 s from equation (11) using the fitted parameters and the isotropic energy $E_{\gamma,\mathrm{iso}}$. The power-law fitting gives (see Fig. 11)

$$L_{10\mathrm{s}} = (4.7 \pm 1.2) \times 10^{48} \, (E_{\mathrm{iso}}/10^{52})^{\,1.3 \pm 0.3}, \qquad (12)$$

and the fitting parameters for each GRB including their uncertainties are shown in Table 7. Furthermore, we estimate the energy released in the GeV band by each GRB in the 0.1–10^4 s time interval, i.e.:

$$E_{0.1-10^4\mathrm{s}} = A_{\mathrm{GRB}} \int_{0.1}^{10000} t^{-1.19} \, \mathrm{d}t \;, \qquad (13)$$

and the derived $E_{0.1-10^4\mathrm{s}}$ are shown in Table 8. The parameters $E_{0.1-10^4\mathrm{s}}$ and $E_{\gamma,\mathrm{iso}}$ (isotropic energy of the prompt emission in γ band) are also correlated by a power-law relation (see Fig. 11):

$$E_{0.1-10^4\mathrm{s}} = (4.4 \pm 1.5) \times 10^{50} \, (E_{\mathrm{iso}}/10^{52})^{1.4 \pm 0.3}. \qquad (14)$$

This positive correlation indicates that the BdHNe I with higher isotropic energy are also more luminous and more energetic in the GeV emission.

9 THE DETERMINATION OF THE MASS AND SPIN OF THE BH IN BDHNE I

The theoretical progress introduced in Ruffini et al. (2019c) has identified the GeV radiation as originating in the *inner engine* of BdHN I. There, for the first time, it has been shown that indeed the rotational energy of a Kerr BH can be extracted for powering an astrophysical system. The *inner engine* is composed of (i) a non-stationary Kerr BH, (ii) a uniform magnetic field of $\sim 10^{10}$G aligned with the rotation axis, and (iii) the presence of a very tenuous fully ionized electron–nuclei plasma. The fundamental new conceptual breakthrough introduced by the physics of the *inner engine* is developed in parallel papers (see e.g. Rueda & Ruffini 2020). The main goal here is to show, using our recently published results, that the rotational energy of the Kerr BH is indeed sufficient to explain the energetics of the GeV emission. In turn, this allows us to determine here the mass and spin of the Kerr BH in each BdHN I.

We here apply the self-consistent solution already well tested in the case of GRB 130427A (Ruffini et al. 2019c) and GRB 190114C (Moradi et al. 2019) for determining the three parameters of the *inner engine*, namely the mass and spin of the BH as well as the strength of the surrounding magnetic field B_0. The values are obtained satisfying three conditions:

(i) The energy budget for the observed GeV luminosity is provided by the extractable rotational energy of a Kerr BH (see equation (1a); see equation 34 in Ruffini et al. 2019c).

(ii) The magnetic field B_0 fulfills the transparency condition for the propagation of the GeV radiation imposed by the e^+e^- pair
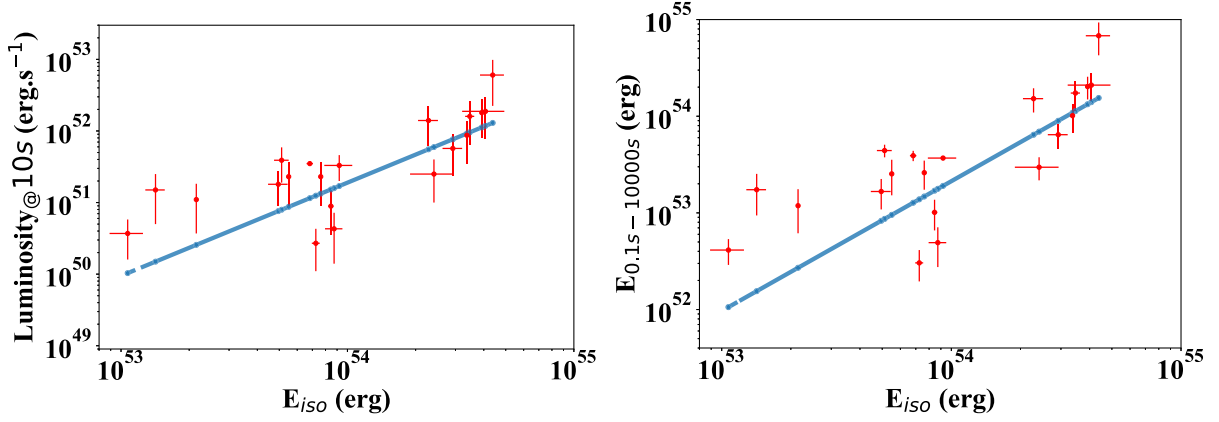
Figure 11. Left: The *Fermi*-LAT luminosity at 10 s in the energy range 0.1–10 GeV versus the isotropic gamma-ray energy from 1 keV to 10 MeV. The BdHNe are listed in Table 7. Right: The *Fermi*-LAT energy from 0.1 to 10^4 s versus isotropic gamma-ray energy from 1 keV to 10 MeV. See the corresponding values in Table 8.

Table 8. Results of $E_{0.1-10^4 s}$ and related error of 20 BdHNe. $E_{0.1-10^4 s}$ is the total GeV energy (in erg) emitted from 0.1 to 10^4 s. GRBs 091127, 091208B, 130518A, 150314A, 150514A are excluded since they have only two data points in their GeV luminosity light curves.

BdHN	$E_{0.1-10^4 s}$	Uncertainty of $E_{0.1-10^4 s}$
080916C	2.1×10^{54}	6.6×10^{53}
090323A	6.8×10^{54}	2.5×10^{54}
090328A	1.73×10^{53}	7.9×10^{52}
090902B	6.4×10^{53}	1.8×10^{53}
090926A	1.54×10^{54}	5.60×10^{53}
091003A	4.12×10^{52}	1.58×10^{52}
100414A	2.53×10^{53}	1.18×10^{53}
100728A	3.0×10^{52}	1.6×10^{52}
110731A	1.6×10^{53}	5.8×10^{52}
120624B	1.7×10^{54}	7.2×10^{53}
130427A	3.6×10^{53}	1.8×10^{52}
131108A	4.4×10^{53}	1.2×10^{53}
131231A	1.2×10^{53}	6.3×10^{52}
141028A	2.6×10^{53}	1.1×10^{53}
150403A	4.9×10^{52}	1.7×10^{52}
160509A	1.1×10^{53}	3.5×10^{52}
160625B	1.1×10^{54}	3.3×10^{53}
170214A	2.1×10^{54}	5.3×10^{53}
170405A	3.0×10^{53}	7.9×10^{52}
180720B	3.8×10^{53}	4.7×10^{52}

Table 9. The mass, M, the spin parameter, $\alpha = J/M^2$, and surrounding magnetic field, B_0 in 11 BdHNe I, out of the 25 long GRBs in Table 5. The high-quality GeV data of this sample allows for a measurement of the lower limit of their 'inner engine' parameters; see equation (1a).

Source	α	$M(\alpha)$ ($M_\odot$)	M_{irr} ($M_\odot$)	B_0 10^{10} G
BdHN I 080916C	0.87	8.9	7.6	1.9
BdHN I 090902B	0.59	5.3	5	2.8
BdHN I 090926A	0.76	8.4	7.7	2.1
BdHN I 110713A	0.37	4.7	4.6	4.5
BdHN I 130427A	0.40	2.3	2.24	4.1
BdHN I 130518A	0.50	2.5	2.4	3.3
BdHN I 131108A	0.56	4.7	4.4	2.9
BdHN I 160509A	0.41	2.4	2.3	4
BdHN I 170214A	0.80	2.8	2.5	2.1
BdHN I 170405A	0.45	3.4	3.3	3.7
BdHN I 180720B	0.27	2.3	2.29	6

production process in the *inner engine* (see equation 35 in Ruffini et al. 2019c).

(iii) The 'quantized' emission of the GeV radiation is determined by the density of the plasma and by the synchrotron radiation time-scale (Ruffini et al. 2019c) (see equation 36 in Ruffini et al. 2019c).

The high-quality GeV data in 11 BdHNe I out of the 25 long GRBs in Table 5 allow us to determine the starting point of the decreasing luminosity, by identifying the transition of the power-law dependence of the GeV luminosity from a positive to a negative slope (see Ruffini et al. 2019c, for more information). This enables us to calculate the lower limit of the mass, M, spin parameter of the BH, α, the corresponding irreducible mass of the BH, M_{irr}, which remains constant during the energy extraction process, and finally the surrounding magnetic field strength, B_0, as reported in Table 9. The values of the masses $M > 2.21\ M_\odot$ and spin parameters of $\alpha < 0.71$ of the BH for BdHNe I presented in Table 9 show the consistency

with the upper limit of the critical mass of the NS in Rhoades & Ruffini (1974) and the mass and spin of rotating NSs computed in Cipolletta et al. (2015); see Fig. 12.

This has indeed been addressed in recent works (Ruffini et al. 2019c), where we have developed a complementary theory and its related analysis to identify the physical conditions that have to be enforced in order to extract the rotational energy of a Kerr BH. We have there addressed an approach of considering a Kerr BH placed in a uniform magnetic field of 10^{10} G aligned along the BH symmetry axis, fulfilling the Einstein–Maxwell equations via the Papapetrou–Wald solution (Papapetrou 1966; Wald 1974) modelling the *inner engine* that produces the MeV, GeV, and TeV radiation and UHECRs as well (Rueda & Ruffini 2020).

10 SPIN-DOWN OF THE BH IN BDHNE I

Following our previous work (Ruffini et al. 2019c), we can turn now from the luminosity expressed in the rest frame of the sources, see equation (11), and from the initial values of the spin and mass of the BH expressed in Section 9, to derive the slowing down of the BH due to the energy loss in the GeV emission.
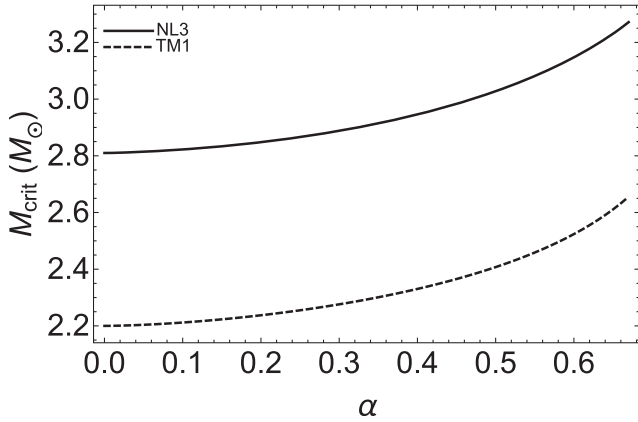
Figure 12. NS critical mass as a function of the spin parameter α for the NL3 and TM1 EOS. We recall that the maximum spin parameter of a uniformly rotating NS is $\alpha_{\max} \approx 0.71$, independently of the NS EOS (see e.g. Cipolletta et al. 2015).

The relation of the luminosity and the extractable rotational energy is (see equation 39 in Ruffini et al. 2019c)

$$L = -\frac{\mathrm{d}E_{\mathrm{extr}}}{\mathrm{d}t} = -\frac{\mathrm{d}M}{\mathrm{d}t}. \tag{15}$$

For each BH during the GeV emission process the M_{irr} is constant. Utilizing the best fit obtained for the GeV luminosity $L_{\mathrm{GeV}} = A_{\mathrm{GeV}}\, t^{-1.2}$ erg s^{-1}, we obtain a relation for the loss of mass energy of the BH by integrating equation (15):

$$M = M_0 + 5At^{-0.2} - 5At_0^{-0.2}, \tag{16}$$

where M_0 is the initial mass of the newborn BH tabulated in Table 9. From the mass–energy formula of the BH, we have (Ruffini et al. 2019c)

$$a = \frac{J}{M} = 2M_{\mathrm{irr}}\sqrt{1 - \frac{M_{\mathrm{irr}}^2}{(M_0 + 5At^{-0.2} - 5At_0^{-0.2})^2}}, \tag{17}$$

where M_0 is the initial mass of the BH presented in Table 9 as M α at time t_0 at which the decaying part of GeV luminosity begins.

As indicative examples, we show in Fig. 13 the decrease of the BH spin, $\alpha = a/M = J/M^2$, as a function of time in GRBs 090902B, 131108A, and 170405A.

The third main results of this paper are: the identification of the rotational energy extraction from a Kerr BH and the consequent measure of the BH mass and spin.

11 CONCLUSIONS

The unprecedented observations of GRBs, pioneered by the *Beppo-Sax* satellite, have developed into the largest ever observational multiwavelength effort in astrophysics: starting with the *Swift*, BAT, and XRT instruments in the X-ray band; see Fig. 14, progressing with the *AGILE* and with *Fermi*-GBM in the MeV–GeV bands. These have worked in synergy with hundreds of optical, radio, and VHE telescopes worldwide including MAGIC (see Fig. 1) and H.E.S.S. (see Fig. 2).

This unprecedented observational effort assisted by parallel theoretical developments has allowed in this article the achievement of a new understanding of three new basic properties of the BdHNe: the first appearance of the SN triggering the entire BdHN process, the SN-rise; the presence of a mildly relativistic afterglow in the

X-ray in *all* BdHN; the identification in *all* BdHN of the origin of the high-energy emission in an *inner engine* driven by a newborn BH; the description of their morphology. We show, for the first time, the extractable energy of a Kerr BH as an astrophysical energy source, which has allowed the inference of the BH mass and spin.

In Section 2, we first recall that binary systems have an important role in understanding both short and long GRBs and we report the progress in the classification of GRBs in nine different subclasses (see e.g. Wang et al. 2019, and references therein). We then focus on the BdHNe: long GRB model with progenitors composed of CO$_{\mathrm{core}}$ and the binary NS companion. The CO$_{\mathrm{core}}$ undergoes gravitational collapses that gives origin to an SN and the collapse of its Fe-core produces a νNS.

We also there recall the fundamental role of the hypercritical accretion of the SN into the companion binary NS and into the νNS determine the BdHNe further evolution (see Fig. 4 and Pisani et al. 2016; Ruffini et al. 2016b, 2018c; Wang et al. 2019 for further details). The SN accretion on to the νNS gives origin to the X-ray afterglow emission, while the SN accretion on to the companion NS leads to different outcomes as a function of the binary period. For periods shorter than 5 min, the hypercritical accretion on to the companion NS is sufficient for the NS to overcome its critical mass and gravitationally collapse to a BH. The BH formation characterizes a BdHN I with an isotropic energy in the range of 10^{52} erg $\lesssim E_{\mathrm{is}} \lesssim 10^{54}$ erg. We here show that it gives origin, *only in some of them*, to the GeV emission observed by *Fermi*-LAT. For larger binary periods, no BH is formed and consequently no GeV radiation is observed, the hypercritical SN accretion leads to an M-NS with an isotropic energy in the range of 10^{50} erg $\lesssim E_{\mathrm{is}} \lesssim 10^{52}$ erg. We refer to these binaries as BdHN II paradigm. The same occurs for more detached binary systems leading to a BdHN III, where the isotropic energy is in the range of 10^{48} erg $\lesssim E_{\mathrm{iso}} \lesssim 10^{50}$ erg.

In Section 3, we have given the spectral properties of the first appearance of the SN-rise in BdHN I and in BdHN II and also differentiate their energetics.

In Section 4, we have related the SN-rise luminosity to the X-ray luminosity of the afterglow in all three BdHNe types. It is a fortunate coincidence that we have recently understood the origin of the afterglow as a consequence of the SN hypercritical accretion on the νNS. This process is dominated by a mildly relativistic synchrotron pulsar-like emission with Lorentz factor $\Gamma \sim 2$ that gives rise to the X-ray afterglow (Ruffini et al. 2018b; Wang et al. 2019; Rueda et al. 2020), and we have also related their X-ray luminosity to the NS spin. This has allowed us to represent in Fig. 8 the afterglows for two BdHNe I, for two BdHNe II, and one BdHN III and estimate in Table 4 the initial spin value of the νNS. What is most remarkable is that the X-ray afterglow is present in *all* BdHN types which implies that, unlike the GeV emission, which as we show in this article to be necessarily beamed, the X-ray afterglow emission is necessarily isotropic. What is equally relevant is that independently of the differences among these four subclasses of BdHN, the X-ray afterglow luminosity emission is consistent with a power-law index of -1.48 ± 0.32 as measured from the *Swift* observations (Pisani et al. 2016), and a common energy source well explained by the rotational energy of the νNS.

The *first main result of this paper* identification of the SN-rise and the measurement of the νNS spin originating the power-law emission of the afterglow (see Figs 7 and 8). The two process of the SN-rise energetics and the νNS dynamics appear to be strongly correlated.

We then turn in Section 5 to consider only the case of BdHN I and their *Fermi*-GBM and LAT observations. In Appendix A, we update
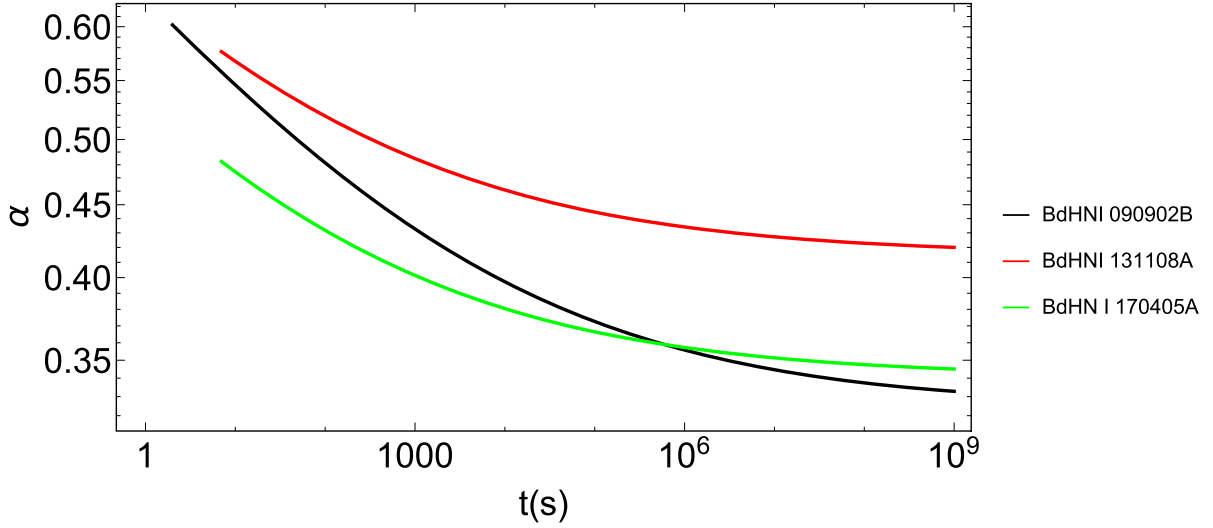
Figure 13. The BH spin as a function of rest-frame time. The initial values of the spin and mass of the BH for GRB 090902B are $\alpha = 0.59$ and $M(\alpha) = 5.3$ $M_\odot$; for 131108A: $\alpha = 0.56$ and $M(\alpha) = 4.7$ $M_\odot$; and for 170405A: $\alpha = 0.45$ and $M(\alpha) = 3.4$ $M_\odot$. This behaviour of the spin parameter indicates that the rotational energy of the BH is decreasing due to the radiation losses in the GeV energy band.
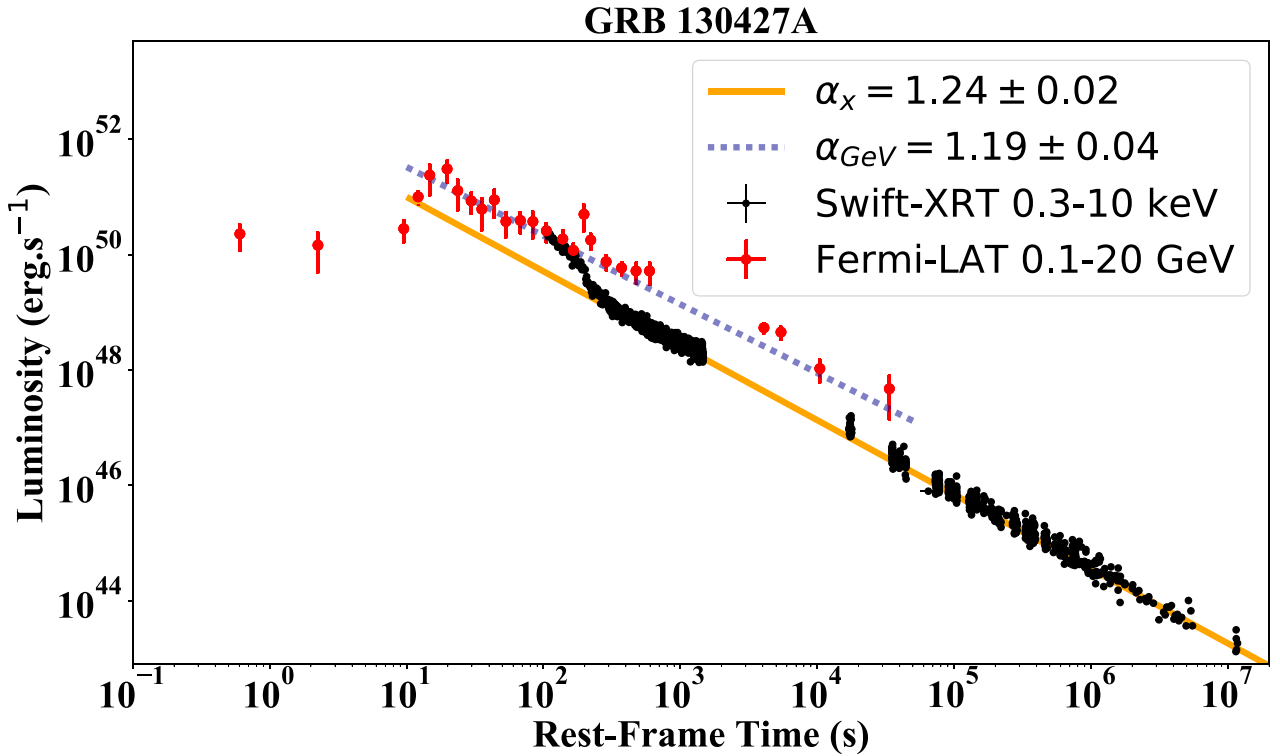
Figure 14. Luminosity of BdHN I 130427A: the black data points represent the rest-frame 0.3–10 keV luminosity obtained from *Swift*-XRT. It follows a decaying power law with amplitude $(3.65 \pm 0.63) \times 10^{52}$ erg s^{-1} and index $\alpha_X = 1.24 \pm 0.02$. The red data points show the rest frame in 0.1–20 GeV luminosity observed by *Fermi*-LAT. It follows a decaying power law with an amplitude of $(5.1 \pm 0.2) \times 10^{52}$ erg s^{-1} and index $\alpha_{GeV} = 1.19 \pm 0.04$. Details are given in Sections 4, 5, and 8.

our previous classification of BdHN I following Pisani et al. (2016), Ruffini et al. (2016b, 2018c) reaching the total number of 378 BdHN I, *all* of them are characterized by

    (i) a measured cosmological redshift;

    (ii) a prompt emission of $T_{90} > 2$ s, measured by *Fermi*-GBM, with isotropic energy larger than 10^{52} erg;

    (iii) a decaying X-ray afterglow, measured by *Swift*-XRT, characterized by a luminosity decreasing with a mean power law with index of $\alpha_X = -1.48 \pm 0.32$.

    Contrary to the case of the X-ray afterglow, universally present in *all* BdHN types, the GeV radiation is present *only in some* BdHN I. No GeV emission occurs in BdHN II and BdHN III. We first explore the possibility that the non-detection of GeV radiation in

some of BdHNe I could be due to the observational limitation of the LAT field of view, i.e. because of the boresight angle smaller than 75°. Indeed, we find that only $N_{tot} = 54$ out of the 378 BdHNe I are inside the boresight angle of *Fermi*-LAT. What is unexpected is that only $N_{LAT} = 25$ out of these 54 BdHNe I exhibit the GeV emission observed by *Fermi*-LAT. For each of these 25 sources, we have given the basic parameters in Table 5. The corresponding data of the remaining 29 BdHN I, without observed GeV radiation, are given in Table 6.

In Section 6, we have assumed that *all* BdHNe I, like all GRBs are homogeneously distributed in space (see e.g. Meegan et al. 1992; Paciesas et al. 1999), we have inferred that the emission of the GeV radiation occurs in two opposite cones each of half-opening angle of ∼60° from the normal to the binary plane.

We duly recall as well that the visualization of the morphology has been made possible thanks to a close collaboration with LANL (see Becerra et al. 2016, 2019, for additional details), leading to the results well illustrated in the simulation presented in Figs 4 and 10. We then conclude from this simulation that all of the 25 LAT sources are actually 'seen from the top' that allows us to fully observe the conical emission of 60° half-opening angle. For the remaining 29 BdHN I without an observed GeV emission, we provide evidence that when the *Swift* data are available, gamma-ray flares and hard and soft X-ray flares as well as extended thermal emissions are observed in these systems (Ruffini et al. 2018a, c), and that these sources have a viewing angle laying in the 'orbital plane' of the binary progenitor system.

We conclude that we are faced with a new morphology of the BdHN I that depends significantly on the viewing angle, 'seen from the top', normal to the binary orbital plane when the GeV emission is observed, or seen 'in the plane' of the binary when the observation of the GeV radiation is impeded by the accreting binary material (see Figs 4, 9, and 10). This is reminiscent of the morphology encountered in some AGNs (see e.g. the AGN IC 310 in Aleksić et al. 2014).

The second main result of this paper is the identification of the BdHN I conical morphology and its explanation within the BdHN I model.

We then recall some theoretical progresses in understanding the origin of the GeV emission:

(i) The identification of the three components of the GRB *inner engine* in GRB 130427A (Ruffini et al. 2019c), composed of a Kerr BH with a magnetic field B_0 aligned with the BH rotation axis, both embedded in a tenuous ionized plasma composed of electrons and ions, has represented a turning point in the study of BdHN I. The electrodynamics of this *inner engine*, based on the Papapetrou–Wald solution (Papapetrou 1966; Wald 1974; Ruffini et al. 2019c), leads to a high-energy emission in two opposite lobes in the MeV, GeV, and TeV radiation as well as narrowly beamed UHECR along the BH polar axis (Moradi et al. 2019).

(ii) This high-energy emission, unlike the traditional models, that implies ultrarelativistic baryonic motion with $\Gamma \sim 10^3$ at 10^{16}–10^{18} cm occurs very close to the BH horizon.

(iii) The energy source is the extractable energy of the BH (Christodoulou 1970; Christodoulou & Ruffini 1971; Hawking 1971, 1972; see equation 1a), and is emitted in a sequence of impulsive process, the '*blackholic quanta*', occurring on a time-scale of 10^{-14} s (Rueda & Ruffini 2020).

On the basis of these results, we have examined the physical origin of the GeV emission observed by *Fermi*-LAT both in BdHN I. We find that the luminosity of the GeV emission as a function of time in the rest frame of the source fulfills a universal decaying power-law

dependence with index of -1.19 ± 0.04; see Fig 3. This has allowed: (1) to verify that indeed the entire GeV radiation observed by *Fermi*-LAT can be energetically expressed in terms of the rotational energy of the Kerr BH; (2) following the procedures in Ruffini et al. (2019c) to evaluate the mass and spin of the BH (see Table 9); and (3) to explicitly compute the slowing down rate of the BH spin due to the GeV emission (see Fig. 13).

It has been possible for some of the 25 sources with the best data:

(i) To compute the lower limit of the initial value of the BH masses, M, and show their consistency with the absolute upper limit of the NS critical mass (Rhoades & Ruffini 1974), and the upper limit of the NS mass of $M = 2.21\ M_\odot$ and spin parameter of $\alpha < 0.71$ computed in Cipolletta et al. (2015).

(ii) To evaluate the value of the spin, a, and show the consistency with the canonical upper limit $\alpha = a/M \leq 1$.

(iii) By combining the value of the spin of the νNS observed from the afterglow (see Table 4), the time intervening between the SN-rise and the UPE phase, the mass estimate of the BH in GRB 190114C and in GRB 090926A and in GRB 180720B, we infer that necessarily in these system we are observing the presence of a BdHN precursor with a companion NS grazing the surface of the CO_{core}.

The third main results of this paper is the identification of the rotational energy extraction from a Kerr BH as the origin of the GeV emission and allowing the consequent measure of the BH mass and spin.

All the above three main results are important: the underlying proof that indeed we can use the extractable rotational energy of a Kerr BH for explaining the high-energy jetted emissions of GRBs and AGNs stands alone. Even more subtle is the fact that the jetted emission does not originate from massive ultrarelativistic jetted emissions, but from very special energy-saving ultrarelativistic quantum and classical electrodynamical processes originating in the high-energy jetted emission. We were waiting for this result for 49 yr, since the writing of equation (1a).

Far from completing an era, GRBs are a fertile ground to discover new physical laws. In front of us: the identification of the nature of the SN-rise, the constituent of the UPE emission, the further application of the *blackholic* energy (Rueda & Ruffini 2020), and the identification of their timescales ranging from 10^{-15} s to 10^{17} s.

ACKNOWLEDGEMENTS

Division at NASA/GSFC and the High Energy Astrophysics Division of the Smithsonian Astrophysical Observatory.

DATA AVAILABILITY

The data underlying this article are available in Appendix A of the article.

REFERENCES

Abdalla H. et al., 2019, Nature, 575, 464
Ackermann M. et al., 2013, ApJS, 209, 11
Aharonian F. et al., 2006, A&A, 457, 899
Aimuratov Y. et al., 2017, ApJ, 844, 83
Ajello M. et al., 2019, ApJ, 878, 52
Aleksić J. et al., 2014, Science, 346, 1080
Aleksić J. et al., 2016a, Astropart. Phys., 72, 61
Aleksić J. et al., 2016b, Astropart. Phys., 72, 76
Amati L. et al., 2000, Science, 290, 953
Atwood W. B. et al., 2009, ApJ, 697, 1071
Barraud C. et al., 2003, A&A, 400, 1021
Barthelmy S. D. et al., 2005, Space Sci. Rev., 120, 143
Becerra L., Cipolletta F., Fryer C. L., Rueda J. A., Ruffini R., 2015, ApJ, 812, 100
Becerra L., Bianco C. L., Fryer C. L., Rueda J. A., Ruffini R., 2016, ApJ, 833, 107
Becerra L., Ellinger C. L., Fryer C. L., Rueda J. A., Ruffini R., 2019, ApJ, 871, 14
Beniamini P., Nava L., Duran R. B., Piran T., 2015, MNRAS, 454, 1073
Berger E., 2014, ARA&A, 52, 43
Blandford R. D., McKee C. F., 1976, Phys. Fluids, 19, 1130
Burrows D. N. et al., 2005, Space Sci. Rev., 120, 165
Campana S. et al., 2006, Nature, 442, 1008
Cano Z., Wang S.-Q., Dai Z.-G., Wu X.-F., 2017, Adv. Astron., 2017, 8929054
Cenko S. B. et al., 2006, ApJ, 652, 490
Cenko S. B. et al., 2011, ApJ, 732, 29
Chand V. et al., 2020, ApJ, 898, 42
Christodoulou D., 1970, Phys. Rev. Lett., 25, 1596
Christodoulou D., Ruffini R., 1971, Phys. Rev. D, 4, 3552
Cipolletta F., Cherubini C., Filippi S., Rueda J. A., Ruffini R., 2015, Phys. Rev. D, 92, 023007
Costa E. et al., 1997, Nature, 387, 783
de Pasquale M. et al., 2006, A&A, 455, 813
Damour T., Ruffini R., 1975, Phys. Rev. Lett., 35, 463
Della Valle M., 2011, Int. J. Mod. Phys. D, 20, 1745
Dominik M., Belczynski K., Fryer C., Holz D. E., Berti E., Bulik T., Mandel I., O'Shaughnessy R., 2012, ApJ, 759, 52
Eichler D., Livio M., Piran T., Schramm D. N., 1989, Nature, 340, 126
Fox D. B. et al., 2005, Nature, 437, 845
Frail D. A., Kulkarni S. R., Nicastro L., Feroci M., Taylor G. B., 1997, Nature, 389, 261
Frontera F. et al., 1998, ApJ, 493, L67
Fryer C. L., Woosley S. E., Hartmann D. H., 1999, ApJ, 526, 152
Fryer C. L. et al., 2007, PASP, 119, 1211
Fryer C. L., Rueda J. A., Ruffini R., 2014, ApJ, 793, L36
Fryer C. L., Oliveira F. G., Rueda J. A., Ruffini R., 2015, Phys. Rev. Lett., 115, 231102
Fujisawa K., Okawa H., Yamamoto Y., Yamada S., 2019, ApJ, 872, 155
Galama T. J. et al., 1998, Nature, 395, 670
Gehrels N. et al., 2005, Nature, 437, 851
Giacconi R., 2003, Rev. Mod. Phys., 75, 995
Giacconi R., Ruffini R., eds, 1978, Physics and Astrophysics of Neutron Stars and Black Holes. North Holland Publishing Co., Amsterdam
Gilkis A., 2018, MNRAS, 474, 2419
Gill P. R., Murray W., Wright M. H., 1981, 500, 136
Giommi P. et al., 2020, A&A, 642, A141
Giuliani A. et al., 2008, A&A, 491, L25

Greiner J. et al., 2009, A&A, 498, 89
Guetta D., Della Valle M., 2007, ApJ, 657, L73
Gursky H., Ruffini R., eds, 1975, Astrophysics and Space Science Library Neutron Stars, Black Holes and Binary X-ray Sources . Springer-Verlag, Berlin
Hawking S. W., 1971, Phys. Rev. Lett., 26, 1344
Hawking S. W., 1972, Commun. Math. Phys., 25, 152
Hewish A., Bell S. J., Pilkington J. D. H., Scott P. F., Collins R. A., 1968, Nature, 217, 709
Hjorth J., Bloom J. S., 2012, The Gamma-Ray Burst - Supernova Connection. Cambridge Univ. Press, Cambridge, p. 169
Hurley K. et al., 2000, ApJ, 534, L23
in 't Zand J. J. M. et al., 1998, ApJ, 505, L119
in't Zand J. J. M. et al., 2001, ApJ, 559, 710
Iwamoto K., Nomoto K., Höflich P., Yamaoka H., Kumagai S., Shigeyama T., 1994, ApJ, 437, L115
Izzo L. et al., 2018, GCN Circ., 23142, 1
Kanbach G., 1996, Mem. Soc. Astron. Ital., 67, 161
Klebesadel R. W., Strong I. B., Olson R. A., 1973, ApJ, 182, L85
Kouveliotou C., Meegan C. A., Fishman G. J., Bhat N. P., Briggs M. S., Koshut T. M., Paciesas W. S., Pendleton G. N., 1993, ApJ, 413, L101
Kumar P., Barniol Duran R., 2009, MNRAS, 400, L75
Li L., 2020, ApJ, 894, 100
Li L.-X., Paczyński B., 1998, ApJ, 507, L59
Li L.-X., Paczyński B., 2000, ApJ, 534, L197
Li L.-X., Paczyński B., 2006, MNRAS, 366, 219
Li L. et al., 2012, ApJ, 758, 27
Li L. et al., 2015, ApJ, 805, 13
Li L., Wang Y., Shao L., Wu X.-F., Huang Y.-F., Zhang B., Ryde F., Yu H.-F., 2018a, ApJS, 234, 26
Li L., Wu X.-F., Lei W.-H., Dai Z.-G., Liang E.-W., Ryde F., 2018b, ApJS, 236, 26
Li L., Ruffini R., Rueda J. A., Moradi R., Wang Y., Xue S. S., 2019, preprint (arXiv:1910.12615)
MAGIC Collaboration, 2019a, Nature, 575, 455
MAGIC Collaboration, 2019b, Nature, 575, 459
Mao S., Paczynski B., 1992, ApJ, 388, L45
Meegan C. A., Fishman G. J., Wilson R. B., Paciesas W. S., Pendleton G. N., Horack J. M., Brock M. N., Kouveliotou C., 1992, Nature, 355, 143
Meegan C. A. et al., 2008, GCN Circ., 8100, 1
Meegan C. et al., 2009, ApJ, 702, 791
Melandri A. et al., 2019, GCN Circ.
Mészáros P., Rees M. J., 1997, ApJ, 482, L29
Metzger M. R., Djorgovski S. G., Kulkarni S. R., Steidel C. C., Adelberger K. L., Frail D. A., Costa E., Frontera F., 1997, Nature, 387, 878
Mirzoyan R., et al., 2019, GCN Circ.
Moradi R., Rueda J. A., Ruffini R., Wang Y., 2019, A&A, preprint (arXiv:1911.07552)
Murdin P., ed., 2000, Compton Gamma Ray Observatory (CGRO). Institute of Physics Publishing, Bristol, p. 4537
Nakamura K., Kuroda T., Takiwaki T., Kotake K., 2014, ApJ, 793, 45
Nappo F. et al., 2017, A&A, 598, A23
Narayan R., Piran T., Shemi A., 1991, ApJ, 379, L17
Narayan R., Paczynski B., Piran T., 1992, ApJ, 395, L83
Nava L., 2018, Int. J. Mod. Phys. D, 27, 1842003
Nomoto K., Hashimoto M., 1988, Phys. Rep., 163, 13
Nousek J. A. et al., 2006, ApJ, 642, 389
Oke J. B. et al., 1995, PASP, 107, 375
Paciesas W. S. et al., 1999, ApJS, 122, 465
Paczynski B., 1986, ApJ, 308, L43
Panaitescu A., 2017, ApJ, 837, 13
Papapetrou A., 1966, Annales de L'Institut Henri Poincare Section (A) Physique Theorique, 4, 83
Pian E. et al., 2000, ApJ, 536, 778
Pisani G. B. et al., 2016, ApJ, 833, 159
Pisani G. B. et al., 2018, in EPJ Web Conf., 168, 04002
Postnov K. A., Yungelson L. R., 2014, Living Rev. Relativ., 17, 3
Racusin J. L. et al., 2011, ApJ, 738, 138

Rees M. J., Meszaros P., 1992, MNRAS, 258, 41

Reifenstein E. C., Brundage W. D., Staelin D. H., 1969, Phys. Rev. Lett., 22, 311

Rhoades C. E., Ruffini R., 1974, Phys. Rev. Lett., 32, 324

Roming P. W. A. et al., 2005, Space Sci. Rev., 120, 95

Rueda J. A., Ruffini R., 2012, ApJ, 758, L7

Rueda J. A., Ruffini R., 2020, Eur. Phys. J. C, 80, 300

Rueda J. A., Ruffini R., Karlica M., Moradi R., Wang Y., 2020, ApJ, 893, 148

Ruffini R., 1974, in Astrophysics and Gravitation: Proceedings of the Sixteenth Solvay Conference on Physics. Editions de l'Universite de Bruxelles, Brussels, p. 349

Ruffini R., 1998, in Sato H., Sugiyama N., eds, Frontiers Science Series 23: Black Holes and High Energy Astrophysics. Universal Academic Press Inc., Tokyo, Japan, p. 167

Ruffini R., Wheeler J. A., 1971, Phys. Today, 24, 30

Ruffini R., Bianco C. L., Fraschetti F., Xue S.-S., Chardonnet P., 2001, ApJ, 555, L117

Ruffini R. et al., 2015a, Astron. Rep., 59, 626

Ruffini R. et al., 2015b, ApJ, 798, 10

Ruffini R. et al., 2016a, ApJ, 831, 178

Ruffini R. et al., 2016b, ApJ, 832, 136

Ruffini R. et al., 2018a, ApJ, 852, 53

Ruffini R., Karlica M., Sahakyan N., Rueda J. A., Wang Y., Mathews G. J., Bianco C. L., Muccino M., 2018b, ApJ, 869, 101

Ruffini R. et al., 2018c, ApJ, 869, 151

Ruffini R. et al., 2019a, preprint (arXiv:e-prints)

Ruffini R., Melon Fuksman J. D., Vereshchagin G. V., 2019b, ApJ, 883, 191

Ruffini R. et al., 2019c, ApJ, 886, 82

Ruffini R., Bianco C. L., Fraschetti F., Xue S.-S., Chardonnet P., 2001, ApJ, 555, L117

Sari R., 1997, ApJ, 489, L37

Sari R., Piran T., 1995, ApJ, 455, L143

Sari R., Piran T., Narayan R., 1998, ApJ, 497, L17

Shirasaki Y. et al., 2008, PASJ, 60, 919

Shklovskij I. S., 1969, Supernovae. Interscience Publishers, New York, NY (USA)

Smith N., Li W., Silverman J. M., Ganeshalingam M., Filippenko A. V., 2011, MNRAS, 415, 773

Staelin D. H., Reifenstein Edward C. I., 1968, Science, 162, 1481

Strong I. B., 1975, Cosmic Gamma-Ray Bursts. D. Reidel Publishing Co., Dordrecht, Holland, p. 47

Tam P.-H. T., He X.-B., Tang Q.-W., Wang X.-Y., 2017, ApJ, 844, L7

Tauris T. M., Langer N., Moriya T. J., Podsiadlowski P., Yoon S.-C., Blinnikov S. I., 2013, ApJ, 778, L23

Tauris T. M., Langer N., Podsiadlowski P., 2015, MNRAS, 451, 2123

Tavani M. et al., 2009, A&A, 502, 995

van Paradijs J. et al., 1997, Nature, 386, 686

Vernet J. et al., 2011, A&A, 536, A105

Wald R. M., 1974, Phys. Rev. D, 10, 1680

Wang Y., Rueda J. A., Ruffini R., Becerra L., Bianco C., Becerra L., Li L., Karlica M., 2019, ApJ, 874, 39

Waxman E., Piran T., 1994, ApJ, 433, L85

Wijers R. A. M. J., Rees M. J., Meszaros P., 1997, MNRAS, 288, L51

Woosley S. E., 1993, ApJ, 405, 273

Woosley S. E., Bloom J. S., 2006, ARA&A, 44, 507

Xu D. et al., 2013, ApJ, 776, 98

Yoon S.-C., Woosley S. E., Langer N., 2010, ApJ, 725, 940

Zhang B., 2018, The Physics of Gamma-Ray Bursts. Cambridge Univeristy Press, Cambridge, UK

Zhang B., Fan Y. Z., Dyks J., Kobayashi S., Mészáros P., Burrows D. N., Nousek J. A., Gehrels N., 2006, ApJ, 642, 354

SUPPORTING INFORMATION

Supplementary data are available at *MNRAS* online.

stab724.pdf

Please note: Oxford University Press is not responsible for the content or functionality of any supporting materials supplied by the authors. Any queries (other than missing material) should be directed to the corresponding author for the article.

This paper has been typeset from a TEX/LATEX file prepared by the author.